Supplementary Information (SI) for Physical Chemistry Chemical Physics.

Supporting Information for the paper: Detailed Kinetic Model for Combustion of NH_3/H_2 Blends

Yu-Chi Kao[a,b], Anna C. Doner[a], Timo T. Pekkanen[a], Chuangchuang Cao[a], Sunkyu Shin[a], Alon Grinberg Dana[c], Yi-Pei Li[b], William H. Green[a,*]

[a] *Department of Chemical Engineering, Massachusetts Institute of Technology, Cambridge, MA 02139*
[b] *Department of Chemical Engineering, National Taiwan University, Taipei, Taiwan*
[c] *Wolfson Department of Chemical Engineering, Technion – IIT, Haifa 3200003, Israel*

---

[*] Corresponding author
Email address: `whgreen@mit.edu` (William H. Green)

1. $\mathbf{H + {}^2H_2NO \longrightarrow H_2 + HNO}$

We were unable to identify a distinct saddle point for the $H + {}^2H_2NO \rightleftharpoons H_2 + HNO$ reaction, possibly because it lies very close to the saddle point of the isomerization channel $NH_3O \rightleftharpoons H_2 + HNO$. Until this saddle point is identified, we recommend using the RMG-estimated [1, 2] rate coefficient provided in Table 1. A preliminary investigation of the triplet-surface $H + {}^2H_2NO \longrightarrow H_2 + HNO(T)$ reaction revealed that it is uncompetitive with other $H + {}^2H_2NO$ reactions. Therefore, this triplet channel was not included in the final kinetic model.

2. $\mathbf{{}^2NO + {}^2H_2NO \longrightarrow 2\,HNO}$ and $\mathbf{{}^3NH + {}^2HO_2 \longrightarrow {}^2NH_2 + {}^3O_2}$

Unpublished conventional transition-state-theory (cTST) calculations were found for these reactions in the RMG database [3]. In the database comments, it is stated that the CCSD(T)-F12/cc-pVTZ-F12//B2PLYPD3/aug-cc-pVTZ level of theory was used for both reactions. Eckart tunneling corrections [4, 5] were presumably included.

3. Hydrogen-abstraction reactions

$$\begin{aligned}
{}^3O_2 + H_2NN &\longrightarrow {}^2HO_2 + {}^2NNH\\
HON + {}^2HO_2 &\longrightarrow {}^2HNOH + {}^3O_2\\
{}^2HO_2 + {}^2HNOH &\longrightarrow H_2O_2 + HON\\
{}^4N + {}^2HNOH &\longrightarrow {}^3NH + HON\\
{}^3NH + {}^2HNOH &\longrightarrow {}^2NH_2 + HON\\
{}^2NO + H_2NN &\longrightarrow HNO + {}^2NNH\\
HON + N_2H_2 &\longrightarrow {}^2NNH + {}^2HNOH\\
2\,{}^2HNOH &\longrightarrow NH_2OH + HON\\
HON + HONO &\longrightarrow {}^2HNOH + {}^2NO_2\\
H + NH_2OOH &\longrightarrow H_2 + {}^2NH_2OO\\
{}^2HO_2 + NH_2OOH &\longrightarrow H_2O_2 + {}^2NH_2OO\\
{}^2NH_2 + NH_2OOH &\longrightarrow NH_3 + {}^2NH_2OO\\
{}^3NH + NH_2OOH &\longrightarrow {}^2NH_2 + {}^2NH_2OO\\
{}^2NH_2OO + NH_2OH &\longrightarrow NH_2OOH + {}^2HNOH
\end{aligned}$$

We performed cTST calculations for these reactions with the Arkane[6] software package, which was interfaced with the Gaussian 16 [7] and Molpro [8, 9] software packages to perform quantum-chemistry computations. The geometries were optimized at the ωB97X-D/Def2-TZVP level of theory [10, 11], and single-point energies were evaluated at the CCSD(T)-F12/cc-pVTZ-F12 level of theory [12]. Hindered-rotor potentials were calculated at the ωB97X-D/Def2-TZVP level of theory. Eckart-tunneling corrections were computed for the reactions.

4. $\mathbf{O({}^3P) + HNO}$

4.1. Quantum Chemistry

The $O({}^3P) + HNO$ reaction was investigated with both coupled-cluster methods and complete active space second-order perturbation theory (CASPT2). The CASPT2 [13], ROHF-CCSD(T) [14], and

ROHF-CCSDT(Q) [15] calculations were run with the ORCA 6.0.1 [16], Gaussian 16 [7], and MRCC [17, 18] software packages, respectively. Stationary-point geometries were first sought and optimized at the CASPT2(14,11)/aug-cc-pVTZ level of theory, and the same level was used to compute harmonic vibrational frequencies. To partially account for anharmonic effects, the computed zero-point energies and harmonic frequencies were scaled by a factor of 0.957 [19]. For the ^{3}HNO$_2$ intermediate, the (14,11) active space consisted of three bonding and anti-bonding sigma orbitals (6,6), the oxygen and nitrogen lone-pair orbitals (6,3), and two radical orbitals on the oxygen (2,2). The corresponding orbitals sets were selected for all other species. Single-point energies were then calculated with the CASPT2(14,11) method using the aug-cc-pVTZ and aug-cc-pVQZ basis sets [12], and the relative-energy differences were extrapolated to the complete-basis-set (CBS) limit with the relation [20]:

$$\Delta E_\infty = \Delta E_{\mathrm{QZ}} - (\Delta E_{\mathrm{TZ}} - \Delta E_{\mathrm{QZ}}) \frac{4^4}{5^4 - 4^4} \ . \tag{1}$$

Single-point energies were calculated with the ROHF-CCSD(T) method using the aug-cc-pVDZ, aug-cc-pVTZ, and aug-cc-pVQZ basis sets. The CBS limit was determined separately for the Hartree-Fock (HF) and the more slowly converging correlation energies. The former and the latter were extrapolated with the [21]

$$E_{\mathrm{HF}}(X) = E_{\mathrm{HF},\infty} + B_{\mathrm{HF}} \mathrm{e}^{-\alpha_{\mathrm{HF}} X} \ , \tag{2}$$

and [22]

$$E_{\mathrm{corr}}(X) = E_{\mathrm{corr},\infty} + B_{\mathrm{corr}} X^{-\alpha_{\mathrm{corr}}} \tag{3}$$

expressions, respectively. In both cases, $X = 2$, $X = 3$, and $X = 4$ correspond to the aug-cc-pVDZ, aug-cc-pVTZ, and aug-cc-pVQZ basis sets, respectively. A system of three equations was solved to determine α, B, and E_∞. The relative energies were further improved with the additive

$$\Delta \mathrm{T(Q)} = \Delta E[\mathrm{CCSDT(Q)} - \mathrm{CCSD(T)}] \tag{4}$$

correction computed with the aug-cc-pVDZ basis set. When performing the coupled-cluster calculations for transition structures, we found that Gaussian and MRCC sometimes converged to a different HF wave function when the default wave-function guesses were used. Given that multi-reference effects are significant for these structures, this behaviour is not surprising. Thus, particular care was taken to ensure that, for a given species, Gaussian and MRCC found the HF wave function that yielded the lowest ROHF-CCSD(T) energy, and then this reference was consistently used in both the ROHF-CCSD(T) and ROHF-CCSDT(Q) evaluations. Note that a wave-function that yielded the lowest HF energy did not necessarily yield the lowest ROHF-CCSD(T) energy. The results of these calculations are tabulated in Table S1 and depicted graphically in Figure S1.

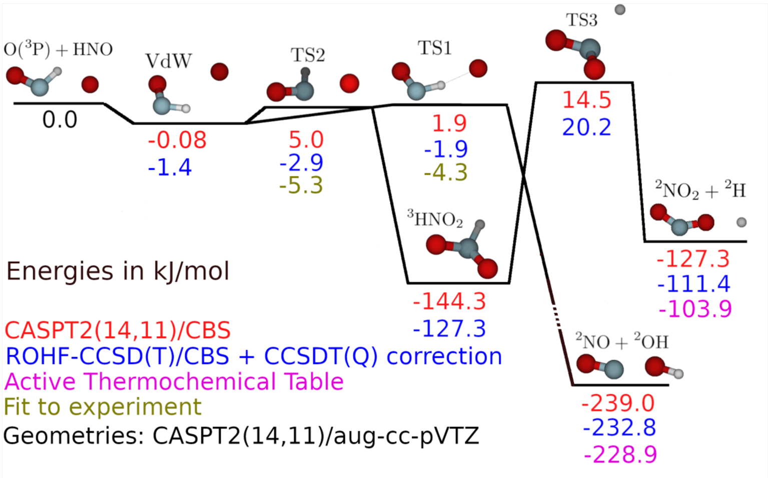

Figure S1: A potential-energy diagram for the O(^{3}P) + HNO reaction system.

Table S1: Stationary-point energies for species on the O(^{3}P) + HNO potential-energy surface. The energies are in kJ mol^{-1}. The tabulated CASPT2(14,11) and ROHF-CCSD(T) values are zero-point-energy corrected. Also listed are the electronic partition functions and symmetry numbers for the species. Spin-orbit effects were accounted for by reducing the energies of the O(^{3}P) + HNO and ^{2}NO + ^{2}OH wells by 0.933 and 1.55 kJ mol^{-1}, respectively.

Species	q_{elec} [a]	$\sigma_{\mathrm{ext}}/m_{\mathrm{opt}}$ [b]	ΔZPE	CASPT2(14,11)/CBS	ROHF-CCSD(T)/CBS[c]	ΔT(Q)[d]	ATcT[e]	Fitted
O(^{3}P) + HNO	q_{O}, 1	1/1, 1/1	0.0	0.0	0.0 (0.016, 0.016)	0	0	-
^{2}NO + ^{2}OH	$q_{^2\mathrm{NO}}$, q_{OH}	1/1, 1/1	-2.3	-239.0	-232.5 (0.024, 0.014)	-0.3	-228.9	-
^{2}NO$_2$ + ^{2}H	2,2	2/1,1/1	-12.6	-127.3	-108.8 (0.027)	-2.6	-103.9	-
^{3}HNO$_2$	3	1/1[f]	12.8	-144.3	-120.1 (0.059)	-7.2	-	-
vdW1(T1)	3 (·2)	1/1	4.4	-0.8	-1.2 (0.018)	-0.2	-	-
vdW1(T2)	-	-	-	2.9	-	-	-	-
vdW1(T3)	-	-	-	11.8	-	-	-	-
vdW2(T1)	3 (·2)	1/2	2.7	1.3	0.4 (0.017)	-0.2	-	-
vdW2(T2)	-	-	-	1.5	-	-	-	-
vdW2(T3)	-	-	-	14.4	-	-	-	-
TS1(T1)	3 (·2)	1/1	-1.0	1.9	0.5 (0.029)	-2.4	-	-4.3 ± 0.2
TS1(T2)	-	-	-	3.4	-	-	-	-
TS1(T3)	-	-	-	15.0	-	-	-	-
TS2(T1)	3	1/2	3.4	5.0	4.4 (0.043)	-7.3	-	-5.3 ± 0.2
TS2(T2)	-	-	-	7.9	-	-	-	-
TS2(T3)	-	-	-	65	-	-	-	-
TS3	3	1/1	-9.9	14.5	29.0 (0.11)	-8.8	-	-

[a] $q_{\mathrm{O}} = 5 + 3\mathrm{e}^{-228\ \mathrm{K}/T} + \mathrm{e}^{-326\ \mathrm{K}/T}$, $q_{\mathrm{NO}} = 2 + 2\mathrm{e}^{-172\ \mathrm{K}/T}$, $q_{\mathrm{OH}} = 2 + 2\mathrm{e}^{-201\ \mathrm{K}/T}$.

[b] Here $\sigma_{\mathrm{ext}}/m_{\mathrm{opt}}$ is the ratio of rotational (external) and optical symmetry numbers.

[c] The values in the parentheses are T1 diagnostics [23].

[d] Approximate CCSDT(Q) correction: variant B [15].

[e] ATcT stands for Active Thermochemical Tables [24].

[f] The inversion motion is explicitly considered, and an internal symmetry number of 2 is applied for this motion.

4.2. Master Equation

Rate-coefficient calculations were performed using the master-equation (ME) solver MESMER 7.1 [25–27]. MESMER is a one-dimensional ME code that treats the total rovibrational energy as the only independent variable; angular-momentum effects are not explicitly considered. For all reactions with saddle-points, the transition state (TS) was placed there. In the $O(^3P) + HNO$ reaction, the reactants first form van der Waals (vdW) complexes before passing over the saddle points that lead to the $^3HNO_2$ and $^2NO + {}^2OH$ products. After applying zero-point-energy (ZPE) corrections, only vdW1 remained below the reactant asymptote, and the corresponding association was found to be barrierless. To obtain the TS state sum for this channel, we performed energy- and angular-momentum–resolved variable reaction coordinate transition state theory (VRC-TST) calculations [28] using Gaussrate version 17-B (Aug. 2, 2017) interfaced with Polyrate [29]. The level of theory used in the VRC-TST calculations was ωB97X-D/cc-pVDZ [10], and the reaction coordinate was defined as the distance (scanned from 3 to 20 Å) between the nitrogen atom in HNO and the approaching $O(^3P)$ atom. The total vdW-complex-forming rate coefficient is well reproduced by the expression

$$k(T) = 4.32 \cdot 10^{-10} \left(\frac{T}{300\ \mathrm{K}}\right)^{-0.371}\ \mathrm{cm^3\,s^{-1}}\ . \tag{5}$$

The two lowest-lying electronic states for the vdW complexes and TS1 are nearly degenerate. To account for this degeneracy, their electronic partition functions were multiplied by a factor of two, yielding a combined electronic degeneracy of six ($3{\cdot}2 = 6$). Of the nine potential-energy surfaces (PESs) that originate from the $O(^3P) + HNO$ reactants, six correlate with the ground-state products of the $O(^3P) + HNO \longrightarrow {}^2NO + {}^2OH$ reaction and three with the $O(^3P) + HNO \longrightarrow {}^3HNO_2$ channel. The rotational symmetry numbers, optical symmetry numbers, and electronic partition functions adopted for all species are summarized in Table S1.

The inclusion of shallow wells such as vdW1 in ME models is undesirable as it leads to overlapping of chemically significant eigenvalues (CSEs) and internal relaxation eigenvalues (IEREs). MESMER uses Bartis-Widom analysis [26, 27] to compute phenomenological rate coefficients, which assumes that CSEs and IEREs are well separated in magnitude. To avoid this problem, the vdW complex was omitted from the final ME model. Instead, effective transition-state sums were determined for the overall $O(^3P) + HNO \longrightarrow {}^2NO + {}^2OH$ and $O(^3P) + HNO \longrightarrow {}^3HNO_2$ reactions with the following expressions:

$$N^{\ddagger}(O(^3P) + HNO \rightleftharpoons {}^2NO + {}^2OH) = \frac{N^{\ddagger}_{\mathrm{loose}} N^{\ddagger}_{\mathrm{TS1}}}{N^{\ddagger}_{\mathrm{loose}} + N^{\ddagger}_{\mathrm{TS1}} + N^{\ddagger}_{\mathrm{TS2}}} \quad \text{and} \tag{6}$$

$$N^{\ddagger}(O(^3P) + HNO \rightleftharpoons {}^3HNO_2) = \frac{N^{\ddagger}_{\mathrm{loose}} N^{\ddagger}_{\mathrm{TS2}}}{N^{\ddagger}_{\mathrm{loose}} + N^{\ddagger}_{\mathrm{TS1}} + N^{\ddagger}_{\mathrm{TS2}}}\ . \tag{7}$$

At lower energies/temperatures ($T < 100$ K), the outer TS is the kinetic bottleneck, whereas at higher temperatures ($T > 100$ K), TS1 and TS2 are rate-determining.

In general, multi-reference effects are significant for the inner TSs (TS1 and TS2 in Table S1), and the relative-energy uncertainties of these saddle points are at least several kJ mol^{-1}. To reproduce the experimental rate data of Inomata and Washida,[30], the heights of these barriers were slightly adjusted, but so that the ROHF-CCSD(T)/CBS + ΔT(Q) energy difference between TS1 and TS2 was kept fixed. The optimal fit required lowering the inner-barrier energies by approximately $2-3$ kJ mol^{-1}— an adjustment well within the expected computational uncertainty. Variational effects were not examined for these inner TSs, although such effects could become relevant at elevated temperatures.

Collisional energy transfer was treated using the single-exponential-down model. The temperature-dependent parameter utilized in this work was

$$\langle \Delta E \rangle^{N_2}_{\mathrm{down}} = 300\ \mathrm{cm^{-1}} \left(\frac{T}{300\ \mathrm{K}}\right)^{0.85}\ . \tag{8}$$

This parameter was found to reproduce experimental fall-off curves for the related $^2NO + {}^2OH \longrightarrow HONO$ reaction [31]. However, in the present case the direct reaction to form $^2NO + {}^2OH$ is overwhelmingly dominant, so the results of the ME simulations are not very sensitive to this parameter. Lennard-Jones (LJ) collision frequencies were calculated using tabulated LJ parameters [32]. For the $^3HNO_2$ intermediate, we chose to use the LJ parameters of N_2O ($\sigma = 3.828$ Å and $\epsilon = 232.4$ K). For N_2 and He, these parameters are $\sigma = 2.551$ Å and $\epsilon = 10.22$ K and $\sigma = 71.4$ Å and $\epsilon = 3.798$ K, respectively

Eckart tunneling corrections were computed for the $^3HNO_2 \longrightarrow {}^2NO_2 + {}^2H$ reaction. For the direct abstraction channel $O(^3P) + HNO \longrightarrow {}^2NO + {}^2OH$ tunnelling corrections were omitted since the corresponding barrier for this appears to be submerged below the reactant asymptote. The master-equation simulations employed an energy-grain size of 25 cm^{-1} and a cut-off energy of 25 k_BT.

5. $H + {}^2H_2NO$

5.1. Quantum Chemistry

The $H + {}^2H_2NO$ reaction was investigated with both coupled-cluster methods and complete-active-space perturbation theory. The CASPT2 and CCSD(T) calculations were run with Molpro 2024.3.0 [8, 9, 33]. Stationary-point geometries were located and optimized at the CCSD(T)/aug-cc-pVTZ level of theory, which was also used to determine harmonic frequencies. The final single-point energies were extrapolated by applying equation 1.

To explore the interaction potential between H and ^2H_2NO radical, approximately 23,000 single-point energies were computed at the CASPT2(12,10)/aug-cc-pVDZ level of theory [34]. These data points are shown in Figures S3 and S4. The (12,10) active space consisted of the single radical orbitals of H and ^2H_2NO (2,2), the three bonding and anti-bonding sigma orbitals of ^2H_2NO (6,6), and the lone-pair orbitals on the oxygen and nitrogen atoms (4,2). In these calculations, the centre-of-mass distance between H and ^2H_2NO was scanned in the range 1.5–10 Å, and at each distance increment, single-point energies were computed for randomly sampled orientations of the fragments. The ^2H_2NO fragment was oriented with a ZYZ Euler rotation matrix using uniformly sampled Euler angles.

Parts of the $2\,H + {}^2H_2NO$ potential-energy surface have been investigated by Klippenstein et al.[35], and when applicable, we directly used their results. They performed VRC-TST channels for the barrierless $^2NH_2 + 2\,OH \rightleftharpoons NH_2OH$ channel, and we utilized their rate-coefficient parameterization for this reaction. We also utilized their results for the $NH_2OH \rightleftharpoons NH_3O$ isomerization reaction. A potential-energy diagram depicting the channels investigated in this work and by Klippenstein et al. is shown in Figure S2. This is the reaction scheme that was used as input in our ME simulations.

Klippenstein et al. also considered the triplet-surface reactions $^2NH_2 + {}^2OH \rightleftharpoons {}^3NH + H_2O$ and $^2NH_2 + {}^2OH \rightleftharpoons NH_3 + O(^3P)$, and we utilize their rate-coefficient parametrizations in our RMG model. In principle, these products could be accessed on the singlet surface through spin-forbidden processes, but we expect them so slow that they need not be included in our model. In any case, performing rate-coefficient calculations for spin-forbidden reactions requires sophisticated methods, and this is beyond the scope of the current work.

Table S2: Stationary-point energies for species on the singlet $H + {}^2H_2NO$ potential-energy surface. The energies are in kJ mol^{-1}. The tabulated ROHF-CCSD(T) values are relative to NH_2OH and zero-point-energy corrected. Also listed are the electronic partition functions and symmetry numbers for the species.

Species	q_{elec}[a]	$\sigma_{\mathrm{ext}}/m_{\mathrm{opt}}$[b]	ΔZPE	ROHF-CCSD(T)/CBS[c]	ΔT(Q)[d]	ATcT[e]
$H + {}^2H_2NO$	2, 2	1/1, 2/1	70.07	322.0 (0.021)	-0.4	319.7 ± 0.62
${}^2NH_2 + {}^2OH$	q_{OH}, 2	2/1, 1/1	72.19	259.1 (0.0082, 0.0087)	0.6	259.3 ± 0.11
$H_2 + HNO$	1, 1	1/1, 1/1	62.62	143.8 (0.0057, 0.016)	-1.6	143.0 ± 0.62
NH_2OH	1	1/1	105.72	0.0 (0.011)	0.0	0.0 ± 0.68
NH_3O	1	3/1	108.04	105.1 (0.014)	0.3	105.3 ± 1.3
$TS(NH_3O \rightleftharpoons H_2 + HNO)$	1, 1	1/1	73.93	310.3 (0.027)	-6.1	N/A

[a] $q_{\mathrm{OH}} = 2 + 2e^{-201\ \mathrm{K}/T}$.

[b] Here $\sigma_{\mathrm{ext}}/m_{\mathrm{opt}}$ is the ratio of rotational (external) and optical symmetry numbers.

[c] The values in the parentheses are T1 diagnostics [23].

[d] Approximate CCSDT(Q) correction: variant B [15].

[e] ATcT stands for Active Thermochemical Tables [24].

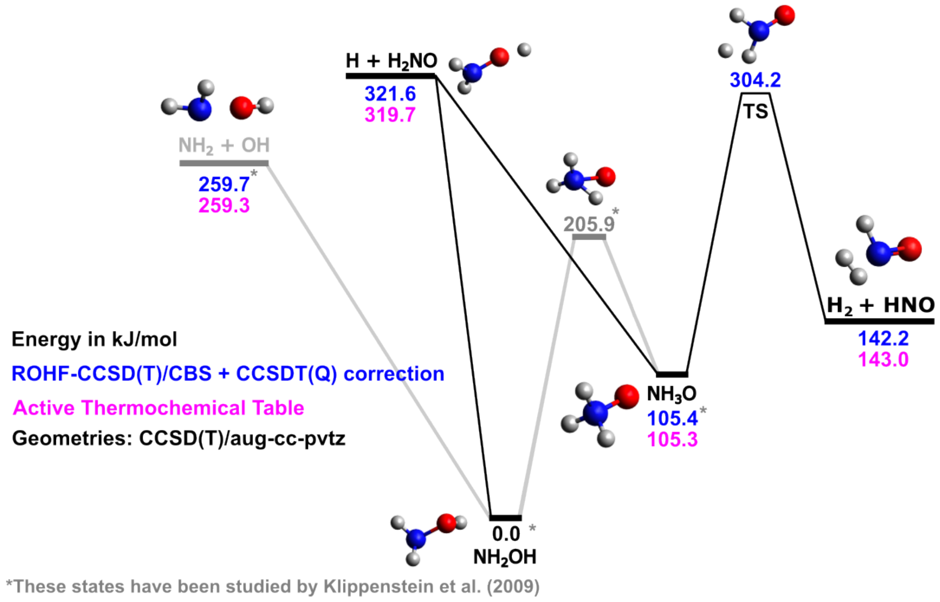

*These states have been studied by Klippenstein et al. (2009)

Figure S2: A potential-energy diagram for the $H + {}^2H_2NO$ reaction system.

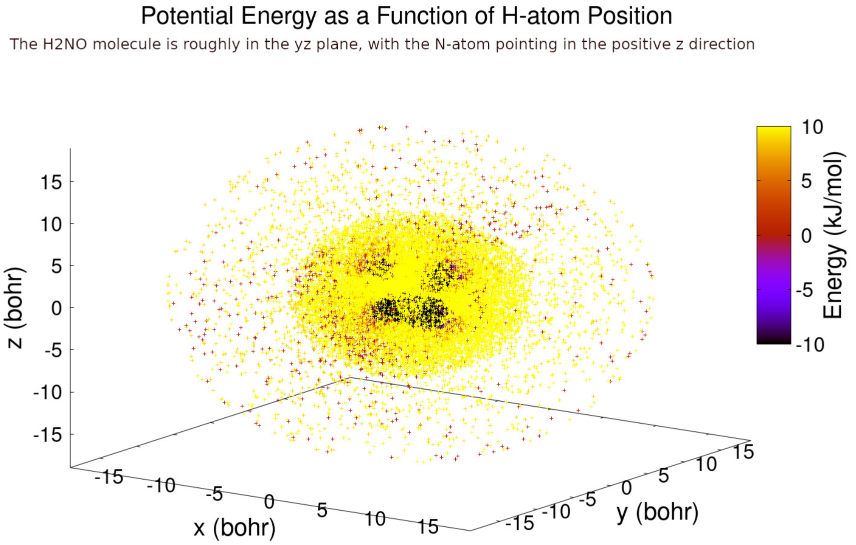

Figure S3: The H + ^2H_2NO interaction potential. The coordinates give the location of the approaching hydrogen atom. The ^2H_2NO fragment's center of mass is located in the origin, and the molecule lies so that it is roughly in the yz plane, with the nitrogen atom pointing in the positive z direction.

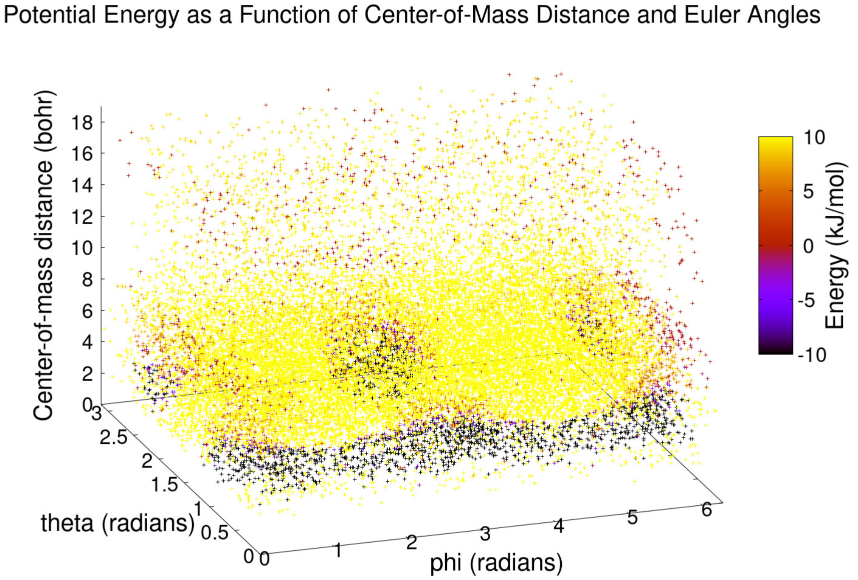

Figure S4: The H + ^2H_2NO interaction potential. The coordinates are the Euler angles that are used to rotate the ^2H_2NO fragment (ZYZ convention). In FTST, Euler angles are used to specify the relative orientation of the fragments.

5.2. Flexible Transition State Theory

For the barrierless H + $^2H_2NO \longrightarrow NH_2OH$ and H + $^2H_2NO \longrightarrow NH_3OH$ reactions, energy- and angular-momentum-dependent TS state sums were evaluated with flexible transition-state theory (FTST) [36]. The custom Julia code used in these calculations is provided in the Supplementary Material. Five pivot points were used. Because the ^2H_2NO radical is approximately planar, two pivot points were placed 0.5 a_0 below and above the nitrogen and oxygen atoms, respectively. For the hydrogen atom, the pivot point coincided with the atom itself. Initial testing revealed that the computed rate coefficients were not very sensitive to the pivot-point distance from the nitrogen or oxygen atoms, so a systematic optimization of this distance was not performed. For a given ^2H_2NO orientation, the reaction coordinate was defined as the pivot-point–to–H-atom distance that maximized the centre-of-mass separation between fragments. The energy and reaction-coordinate grids were chosen as $3.17 \cdot 10^{-6} - 1.98 \cdot 10^{-1}$ Hartree and 1.0–25 Å, respectively. The angular-momentum grid range depended on total energy: at low energies, it was only a few $\hbar$, while at the highest considered energy it was 0–250 $\hbar$. Each grid contained 100 points, with logarithmic spacing used for the energy grid. An electronic-degeneracy factor of 1/4 was applied to the obtained state sums.

5.3. Master Equation

Final rate coefficients were calculated with the master-equation solver implemented in Arkane [6]. Stationary-point data calculated at CCSD(T)/CBS//CCSD(T)/aug-cc-pVDZ for the $NH_2OH \rightleftharpoons NH_3O$ isomerization was adopted from Klippenstein et al. [35]. For the barrierless reactions, the inverse Laplace transform (ILT) approach was employed to determine TS state sums.[37, 38] The ILT technique requires as input the modified Arrhenius parameters of the reaction's canonical rate coefficient. Accordingly, our FTST-derived rate coefficients were parameterized in modified Arrhenius form, and for the $NH_2OH \rightleftharpoons {}^2NH_2 + {}^2OH$ dissociation, we used the Arrhenius expression reported by Klippenstein et al. [35]. For the collision model, Lennard-Jones (LJ) parameters were taken from the RMG-database [3] or estimated with RMG [1, 2]. All parameters are provided in the accompanying Arkane `input.py` file. Collisional energy transfer was described by the single-exponential-down model using the temperature-dependent parameter

$$\langle \Delta E \rangle_{\mathrm{down}}^{\mathrm{N_2}} = 300\ \mathrm{cm}^{-1} \left(\frac{T}{298\ \mathrm{K}} \right)^{0.85} . \tag{9}$$

The modified strong collider method was used with a maximum energy grain size of 4.184 kJ mol^{-1}, a pressure range 0.01–100.0 bar, and a temperature range 300–2000 K. The rates were fitted to pressure-dependent Arrhenius expressions. Figures S5 and S6 show the computed rate coefficients for the $^2NH_2 + {}^2OH$, H_2 + HNO, NH_2OH, and NH_3O product channels at various temperatures and pressures. Neither NH_2OH nor NH_3O exhibits significant stabilization: under all conditions up to 100 bar, the rates for the well-skipping channel $^2NH_2 + {}^2OH$ dominate those for the stabilized NH_2OH and NH_3O products.

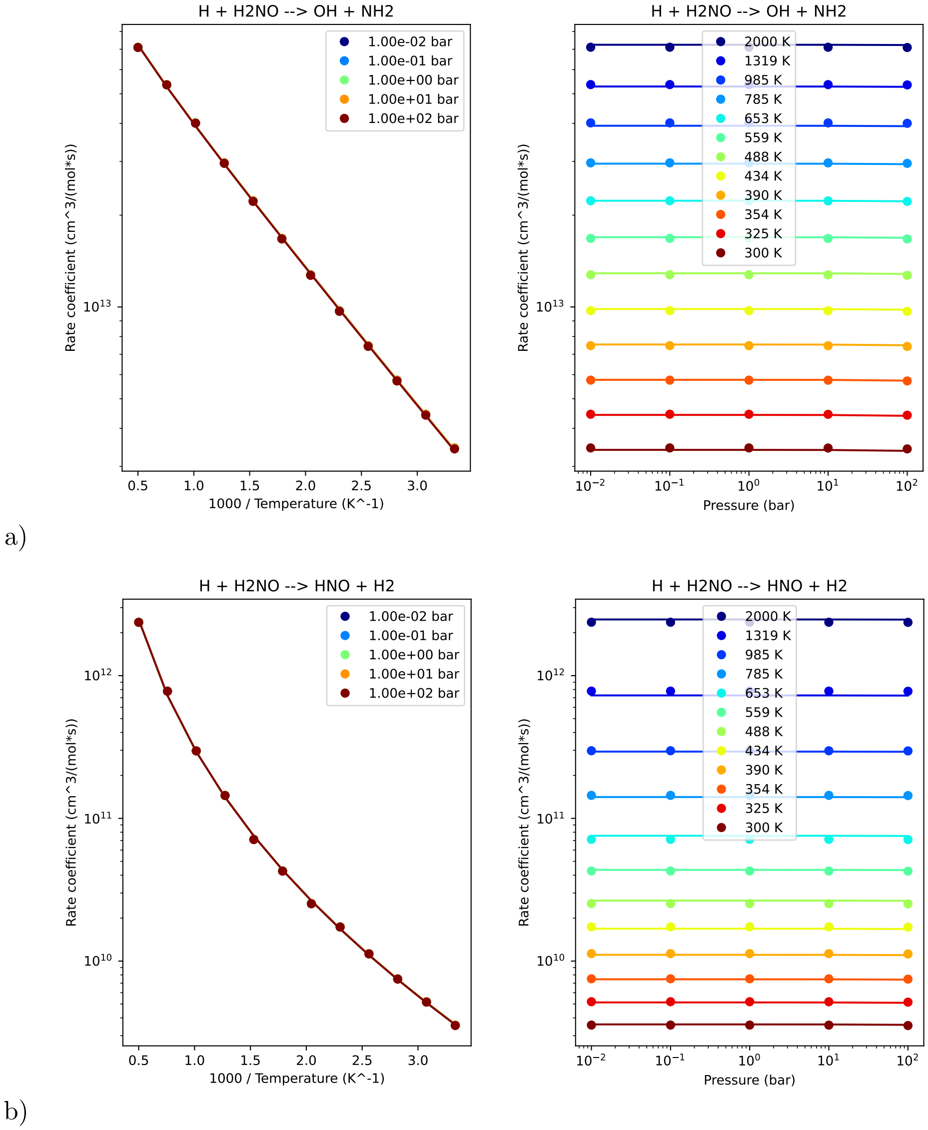

Figure S5: Pressure-dependent rate coefficients for $H + {}^2H_2NO \longrightarrow {}^2NH_2 + {}^2OH$ and $H + {}^2H_2NO \longrightarrow H_2 + HNO$.

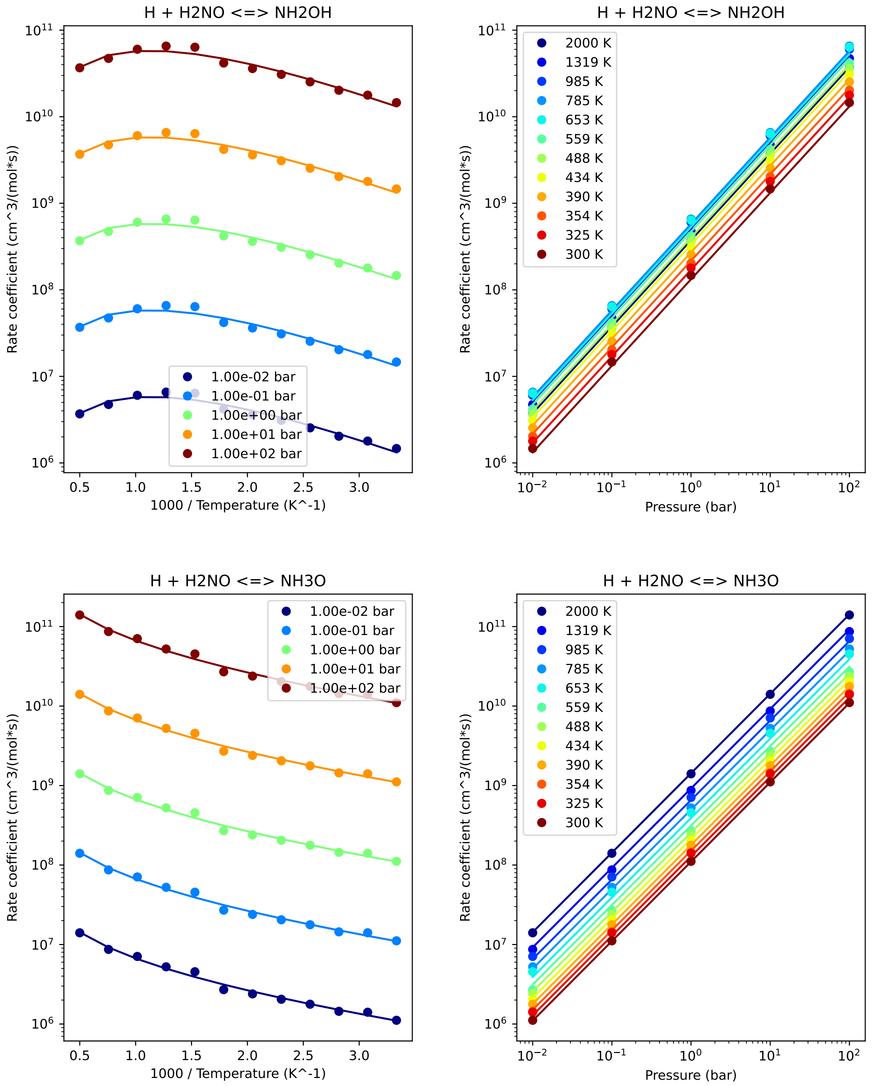

Figure S6: Pressure-dependent rate coefficients for $H + {}^2H_2NO \longrightarrow NH_2OH$ and $H + {}^2H_2NO \longrightarrow NH_3O$.

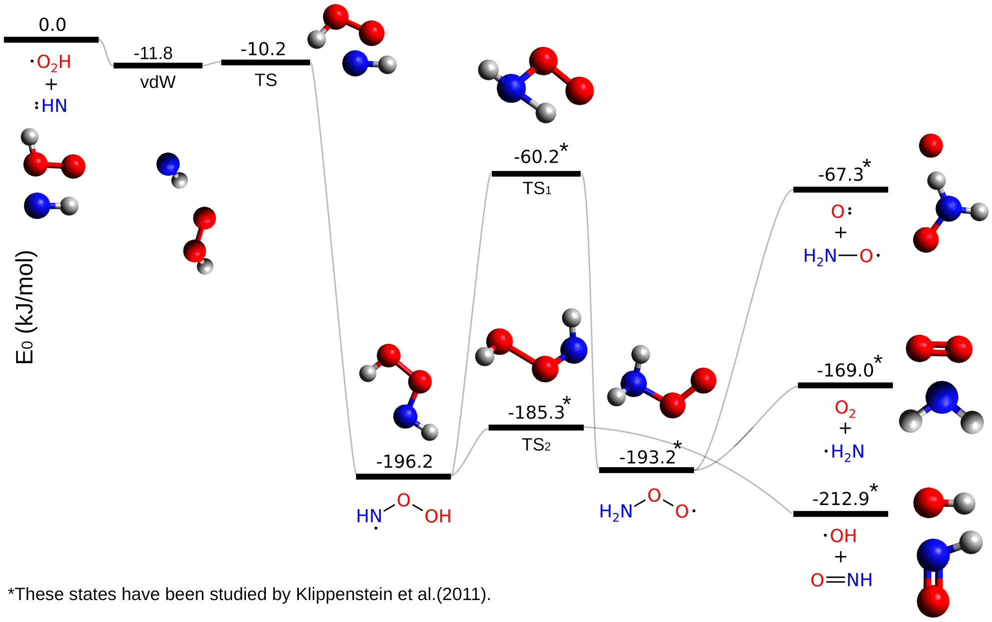

*These states have been studied by Klippenstein et al.(2011).

Figure S7: Potential-energy diagram for the $^2HO_2 + {}^3NH$ reaction system calculated at the CASPT2(7,7)/CBS level of theory. All energies are given relative to the separated reactants. For states marked with an asterisk (*), we use the relative energies and geometries reported by Klippenstein et al.[39]

6. $^2\mathbf{HO_2} + {}^3\mathbf{NH}$

Stationary-point geometries and harmonic frequencies were determined at the CASPT2(7,7)/aug-cc-pVDZ level of theory. This active space consisted of the bonding and anti-bonding σ orbitals for the O−O and O−H bonds (4,4) and the radical orbitals on $^2HO_2$ and ^3NH (3,3). Hindered-rotor potentials were calculated at the ωB97X-D/Def2-QZVP level of theory. Single-point energies were evaluated at the CASPT2(7,7)/aug-cc-pVTZ and CASPT2(7,7)/aug-cc-pVQZ levels of theory, and the electronic energy was extrapolated to the complete-basis-set CBS limit using the

$$\Delta E_\infty = \Delta E_{\mathrm{QZ}} - (\Delta E_{\mathrm{TZ}} - \Delta E_{\mathrm{QZ}})\,\frac{4^4}{5^4 - 4^4}\ . \tag{10}$$

relation.[20] Only the $^2HO_2 + {}^3NH \longrightarrow$ vdW complex $\longrightarrow {}^2NHOOH$ channel was investigated with quantum-chemistry methods in this work. For the other stationary points in the reaction system, we used the relative energies and geometries reported by Klippenstein et al. [39]. The system's potential-energy diagram is shown in Fig. S7.

For the $^2HO_2 + {}^3NH \longrightarrow {}^2NHOOH$ association reaction, the reactants first form a vdW complex, after which the ^2NHOOH product is formed by passing over a submerged saddle point. At low temperatures, the vdW-forming TS (outer TS) is the kinetic bottleneck, but at high temperatures, the TS is in the vicinity of the submerged barrier (inner TS). Our testing revealed that at $T > 400$ K the kinetics are entirely determined by the inner TS. Thus, to compute the $^2HO_2 + {}^3NH \longrightarrow {}^2NHOOH$ rate coefficient, we performed cTST calculations with the TS placed on the submerged saddle point. The details of the ME simulations are the same as for $H + {}^2H_2NO$.

Pressure effects are negligible for this system. At realistic pressures, an energized ^2NHOOH adduct is never stabilized, and it instead rapidly decomposes to form $^2OH + HNO$. Even at 100 bar, the well-skipping $^2HO_2 + {}^3NH \longrightarrow {}^2OH + HNO$ channel is overwhelmingly dominant.

7. Comparison of Updated Rate Coefficients with Existing Mechanisms

To assess the relevance and impact of the newly computed kinetics, we compare the *ab initio* rate coefficients obtained in this work with those adopted in existing NH_3 oxidation mechanisms when such data are available. Table 1 of the main manuscript lists all reactions for which new or updated Arrhenius parameters were derived in this work (entries marked "pw"). Among these reactions (R16–R32 and R36–R40), only three reactions are explicitly included in previously published NH_3 mechanisms examined here (CRECK, NUIG, and KAUST). These reactions are:

- R16: $NO + H_2NO \longrightarrow 2\,HNO$
- R31: $O + HNO \longrightarrow OH + NO$
- R37: $H + H_2NO \longrightarrow NH_2 + OH$

For all remaining reactions in Table 1, no prior rate expressions exist in the mechanisms considered; consequently, the present *ab initio* calculations provide the first available rate coefficients for these channels within detailed NH_3 combustion mechanisms. Figure S8 compares the newly computed rate coefficients for reactions R16, R31, and R37 with those adopted in the CRECK, NUIG, and KAUST mechanisms.

All mechanisms considered adopt the same empirical rate expression for $NO + H_2NO \longrightarrow 2\,HNO$, originally estimated by Miller and co-workers and reported by Glarborg et al. (2018)[40]. In contrast, the present work provides the first *ab initio*–derived rate coefficient for this reaction. As shown in Figure S8 (a), the calculated rate coefficients are systematically lower than the empirical estimate over the temperature range 700–1900 K. The discrepancy is most pronounced at low temperatures, where the legacy expression overpredict the rate by nearly an order of magnitude.

The CRECK, NUIG, and KAUST mechanisms all employ a temperature-independent rate coefficient for $O + HNO \longrightarrow OH + NO$, derived from the low-temperature experimental measurements of Inomata and Washida (1999) [41]. In that study, rate coefficients were measured over the limited temperature range of 242–473 K and subsequently extrapolated to combustion conditions. Figure S8 (b) compares this temperature-independent expression with the *ab initio* rate coefficient computed in the present work. The calculated rate exhibits weak U-shaped temperature dependence that reaches its minimum around 550 K. Despite the different functional form, the resulting deviations from the literature expression remain within approximately a factor of two at combustion-relevant temperatures, explaining why the rate has performed reasonably in practical simulations.

For the $H + {}^2H_2NO \longrightarrow {}^2NH_2 + {}^2OH$ reaction, the CRECK and KAUST mechanisms employ a temperature-independent abstraction rate based on early estimation and analogy arguments. The commonly used value ($A \approx 4\times10^{13}\ \mathrm{cm^3\,mol^{-1}\,s^{-1}}$) originates from hydrocarbon analogies and predates modern electronic-structure studies of the ${}^2H_2NO$ system proposed by Baulch et al. (1992). The NUIG-2024 mechanism does not include the forward reaction explicitly, but instead derives it from a reverse estimated rate combined with thermochemical data, introducing additional uncertainty. In contrast, the present work provides the first direct *ab initio*, temperature-dependent forward rate coefficient for this reaction over combustion-relevant temperatures. As shown in Figure S8(c), the computed rate coefficient displays a markedly different temperature dependence from those adopted in existing mechanisms.

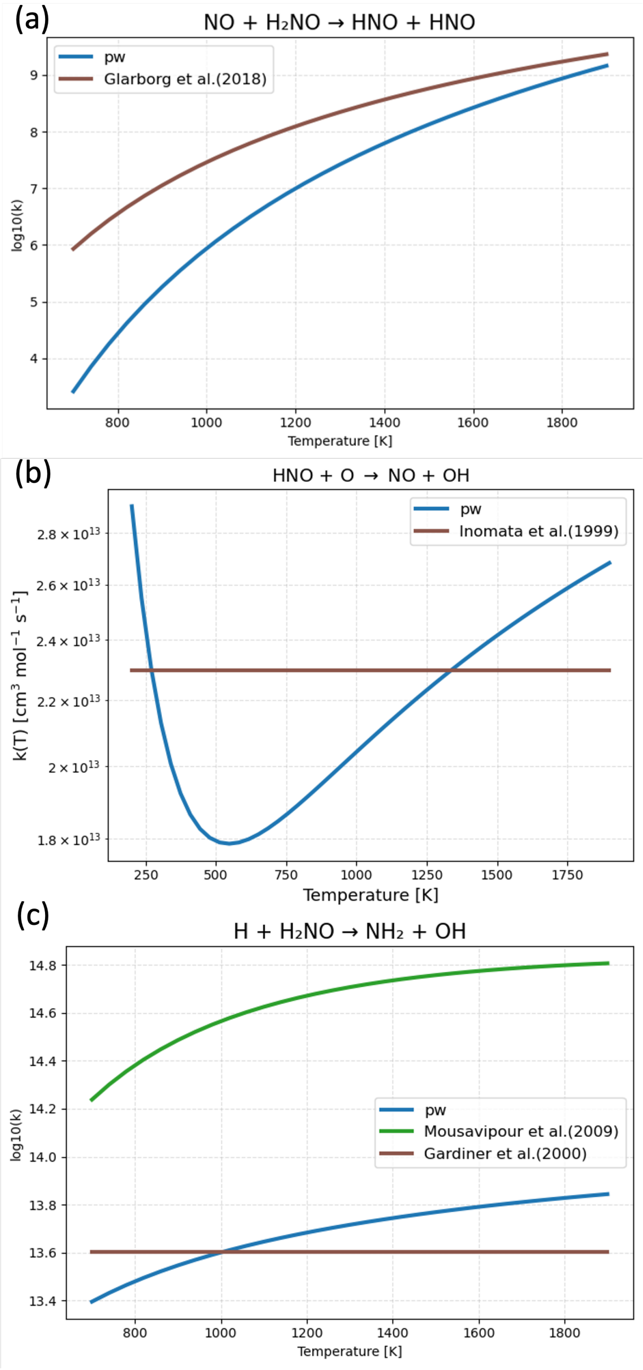

Figure S8: Comparison of newly computed *ab initio* rate coefficients (pw, blue) with rate expressions adopted in existing NH_3 oxidation mechanisms. (a) $NO + H_2NO \longrightarrow 2\,HNO$: comparison with the empirical estimate reported by Glarborg et al. (2018),[40] used in the other mechanisms. (b) $O + HNO \longrightarrow OH + NO$: comparison with the temperature-independent rate derived from low-temperature experiments by Inomata and Washida (1999) [41]. (c) $H + H_2NO \longrightarrow NH_2 + OH$: comparison with the temperature-independent estimate used in the CRECK and KAUST mechanisms (Gardiner et al., 2000)[42] and the theoretical expression adopted in NUIG-2024 (Mousavipour et al., 2009) [43]. The present calculations provide the first direct, temperature-dependent forward rate coefficient for this reaction across combustion-relevant temperatures.

8. Model Validation with $NH_3/H_2/C_1$ Mechanisms

We also provide additional model-validation comparisons using several recently published NH_3–H_2 mechanisms that include extended C_1 (and broader hydrocarbon) submechanisms, namely those of Huang et al.[44], Zhang et al.[45], and Shrestha et al.[46]. These mechanisms were developed to address ammonia combustion in broader fuel contexts (e.g., co-firing with hydrocarbons, syngas, or methane-containing streams) and therefore extend beyond the N/H/O chemical space that is the primary focus of the present work.

The objective of this work is to isolate and assess the impact of updated N/H/O kinetics on NH_3/H_2 oxidation; accordingly, the primary benchmarking set in the main manuscript is restricted to mechanisms developed specifically for N/H/O chemistry. The comparisons shown here are provided for completeness and transparency. However, because these NH_3–H_2–C_1 mechanisms include additional hydrocarbon chemistry and were not developed under the same N/H/O-only scope, they are not used to draw the mechanistic conclusions discussed in the main text. Nevertheless, extending the present mechanism to incorporate C_1 chemistry for broader-fuel applications is an active direction of our ongoing work.

8.1. Ignition Delay Time

Figure S9 and S10 compare ignition delay time (IDT) predictions from the NH_3–H_2–C_1 mechanisms against the same shock-tube datasets used in the main manuscript (Figures 7 and 8), including both pure NH_3 and NH_3/H_2 mixtures. Overall, the C_1-extended mechanisms reproduce the major trends in ignition delay with temperature, pressure, and blending ratio, and their predictions fall within the general spread observed among N/H/O-focused mechanisms.

The Zhang_2023 mechanism shows behaviour similar to that of KAUST_2023 in the main text, as both originate from the same study.[45] In the present Supporting Information comparison, however, we employ the more comprehensive NH_3–NOx–C_1_complete mechanism in their Supporting Information, which contains a substantially larger reaction set. By contrast, the main-text comparison in Section 3.4 uses the NH_3–NOx–CO–H_2 mechanism. Despite this expanded chemical scope, the resulting IDT predictions remain very close to those obtained with the KAUST_2023 mechanism used in Section 3.4, indicating that the inclusion of additional C_1 chemistry does not significantly alter ignition behaviour under the conditions examined here. Among the C_1-extended mechanisms considered, the Shrestha_2025 model provides the closest agreement with the atmospheric-pressure pure-NH_3 ignition-delay measurements of Chen et al. In contrast, for NH_3/H_2 mixtures, the Shrestha_2025 mechanism tends to underpredict ignition delay times across most conditions. Based on this extended validation, the RMG and RMG_Burke mechanisms continue to provide among the most balanced and consistent IDT predictions across the full range of pressures, temperatures, and blending ratios considered. Notably, this performance is achieved without empirical tuning of rate coefficients, reinforcing the robustness of the N/H/O-focused kinetic framework adopted in this work.

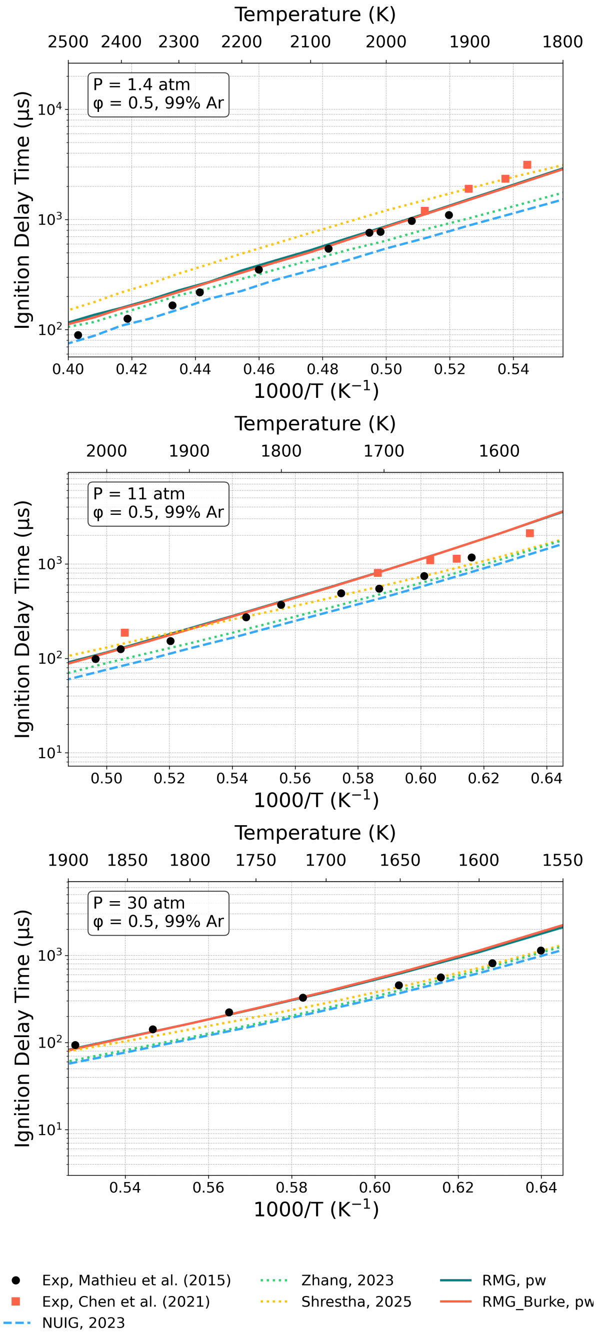

Figure S9: The NH_3 IDT predictions of the current RMG mechanisms and recently developed literature mechanism [44–46] compared with experimental data.[47, 48]

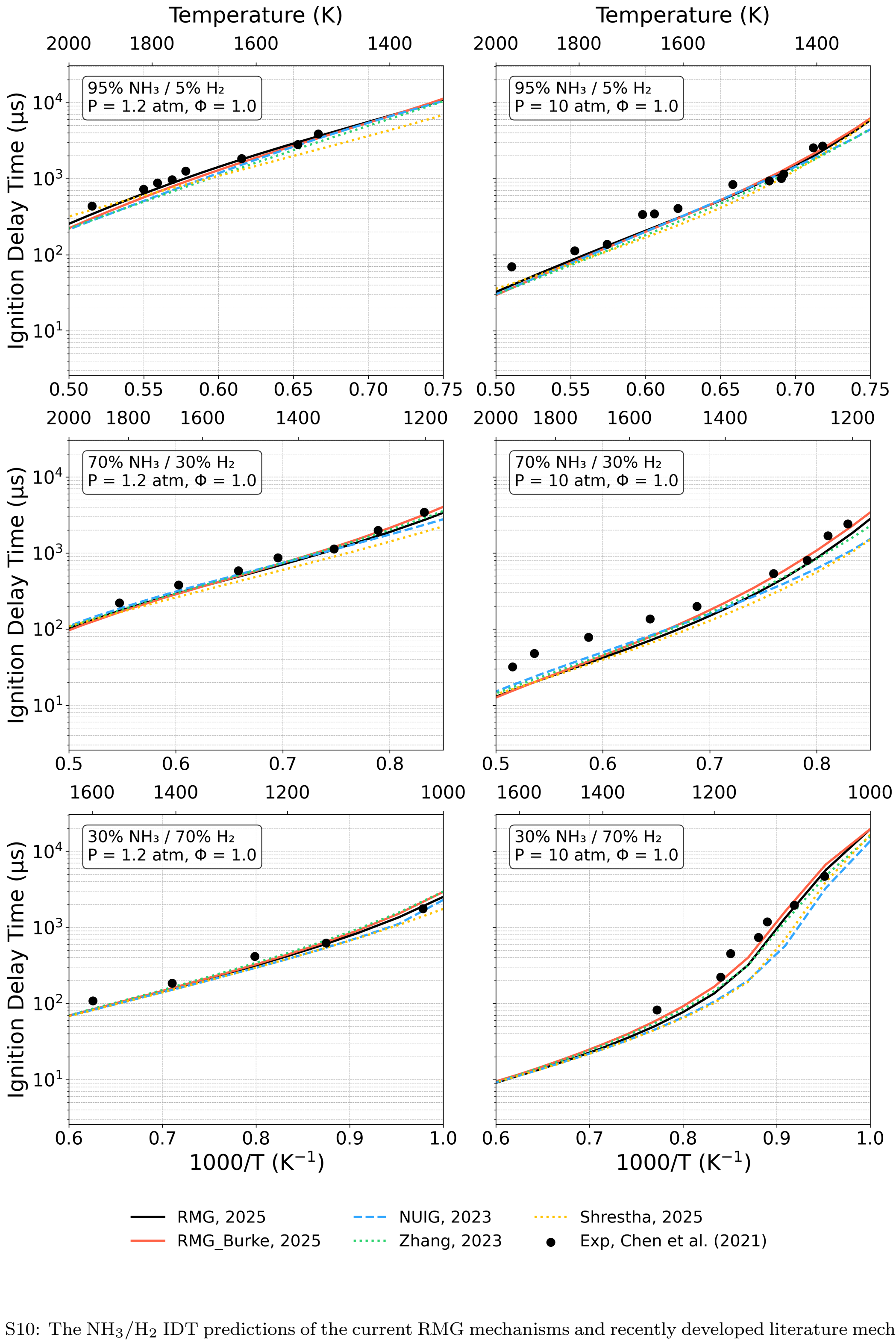

Figure S10: The NH_3/H_2 IDT predictions of the current RMG mechanisms and recently developed literature mechanisms [44–46] compared with experimental data.[48]

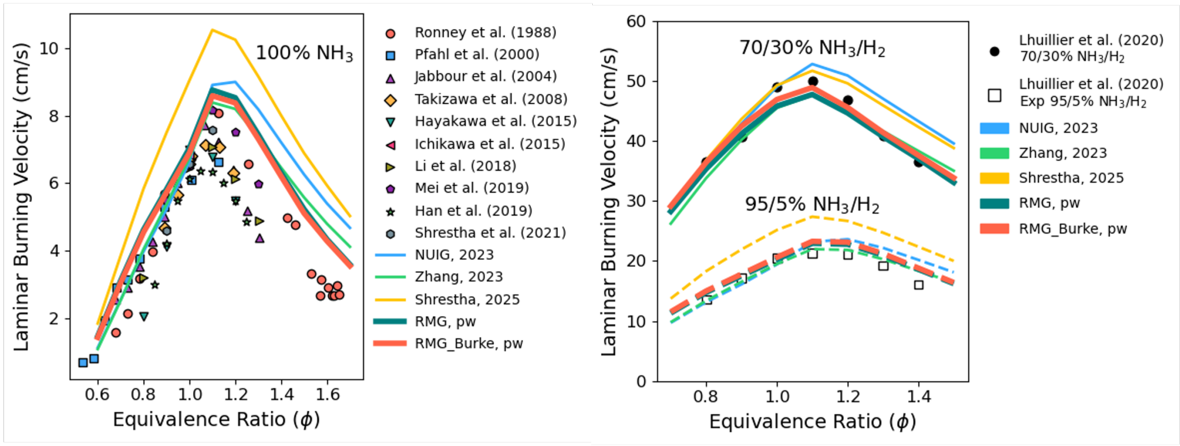

Figure S11: The NH_3/H_2 LBV predictions of the current RMG mechanisms and recently developed literature mechanisms [44–46] compared with experimental data for pure NH_3,[49–58] and NH_3/H_2 mixtures.[59]

8.2. Laminar-Burning Velocity

Figure S11 compares experimental and model-predicted laminar-burning velocities (LBVs) for pure NH_3 and NH_3/H_2 mixtures with air at atmospheric pressure, unburned-gas temperatures of 298K and 473K. In response to a reviewer's suggestion, additional comparisons are included here using recently published NH_3–H_2 mechanisms that contain extended C_1 submechanisms[44–46], together with the present RMG and RMG_Burke mechanisms.

For pure NH_3 flames, all mechanisms predict a peak LBV at a slightly fuel-rich equivalence ratio ($\phi \approx 1.1$), consistent with experimental observations. Zhang_2023 and NUIG_2023 accurately reproduce the flame speeds under lean and near-stoichiometric conditions ($\phi \leq 1.0$), but systematically overpredict LBVs in the fuel-rich regime ($\phi > 1.0$), in agreement with the trends observed for the five reference mechanisms compared in the main manuscript. Among the C_1-extended mechanisms, Shrestha_2025 consistently overpredicts LBVs across the full equivalence-ratio range, with peak values exceeding those of the RMG_Burke mechanism by more than 20% at $\phi \approx 1.1$. The Zhang_2023 mechanism yields the closest agreement with experimental data among the C_1-extended models, but still exhibits larger deviations than the RMG_Burke mechanism, particularly under fuel-rich conditions. Overall, the RMG_Burke mechanism continues to provide the closest agreement with experimental LBVs across the full equivalence-ratio range, particularly under fuel-rich conditions ($\phi > 1.1$), consistent with the conclusions drawn in the main manuscript.

Blending hydrogen with ammonia substantially increases the laminar-burning velocity, thereby enhancing flame stability and practical combustibility. However, the Shrestha_2025 mechanism continues to overpredict LBVs for the 95/5 NH_3/H_2 mixture across the full equivalence-ratio range.

8.3. Oxidation in a Jet-Stirred Reactor (JSR)

Figure S12 compares simulated species profiles for pure NH_3 oxidation in a jet-stirred reactor with experimental measurements from Zhang et al. [60] and Osipova et al. [61]. Results from the present RMG and RMG_Burke mechanisms are shown together with several recent literature mechanisms for reference.

For NH_3 consumption and H_2O formation, all mechanisms reproduce the overall temperature-dependent trends observed experimentally. Compared to the RMG and RMG_Burke models, several literature mechanisms predict an earlier onset of NH_3 consumption, leading to a larger deviation from the experimental ignition temperature. The RMG and RMG_Burke mechanisms provide among the closest agreement with the experimental onset for both NH_3 depletion and H_2O formation.

For ^{2}NO, all mechanisms predict increasing concentrations above approximately 1200 K. However, the literature mechanisms generally yield higher ^{2}NO levels than the RMG-based models in this temperature range. In particular, the Shrestha_2025 mechanism predicts ^{2}NO concentrations that are nearly a factor of two higher than those obtained with the RMG and RMG Burke mechanisms, indicating substantial sensitivity to the underlying nitrogen-chemistry pathways at elevated temperatures.

The disagreement is more pronounced for N_2O. The NUIG, RMG, and RMG_Burke mechanisms substantially overpredict the peak N_2O mole fraction and exhibit broader N_2O formation regions than observed experimentally. In contrast, the Shrestha_2025 mechanism provides the closest agreement with the measured N_2O profile, while the Zhang_2023 mechanism slightly underpredicts the experimental peak. These results indicate persistent uncertainties in the N_2O-forming and -consuming reaction pathways under JSR conditions.

Overall, the JSR validation for pure NH_3 demonstrates that the present mechanisms robustly capture the major features of ammonia consumption and oxidation, while notable discrepancies remain for ^{2}NO and especially N_2O.

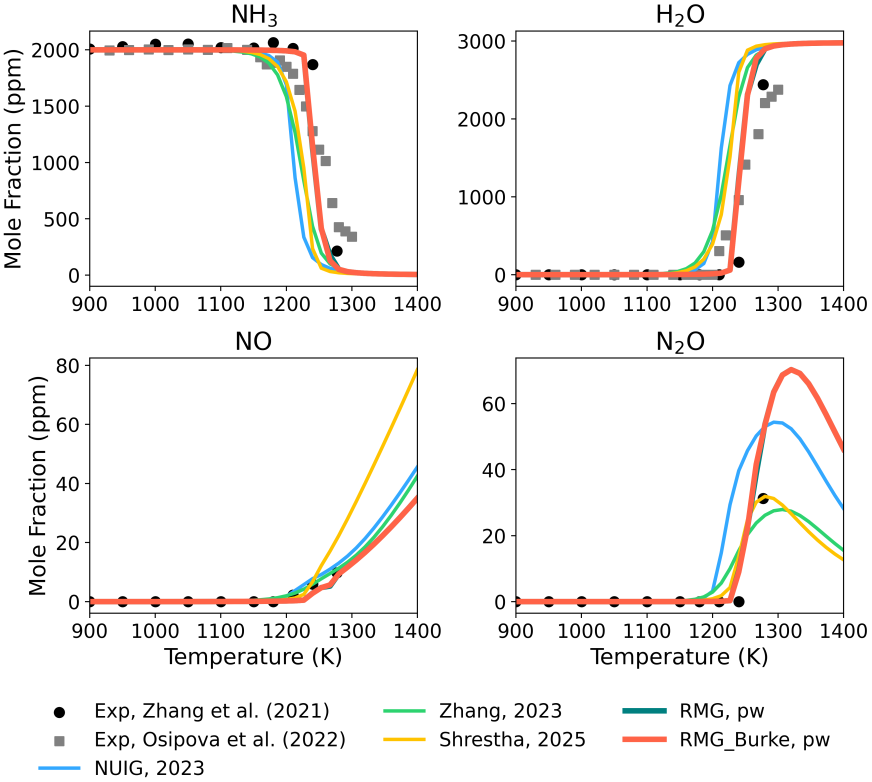

Figure S12: RMG-generated mechanism and representative literature mechanisms [44–46] comparisons against species profiles in JSR oxidation of pure NH_3 [60, 61].

Figure S13 shows the corresponding JSR species profiles for the 90 % NH_3 / 10 % H_2 mixture under otherwise identical conditions. Overall, the addition of a small amount of H_2 does not substantially alter the relative performance trends among the mechanisms, but it slightly shifts the onset of oxidation to lower temperatures.

For NH_3 consumption and H_2O formation, all mechanisms predict nearly overlapping profiles across the temperature range considered. The Shrestha_2025 mechanism exhibits a modest deviation in the intermediate-temperature regime (approximately 1050–1200 K), where it slightly overpredicts the NH_3 mole fraction and correspondingly underpredicts H_2O formation. By contrast, the RMG and RMG

Burke mechanisms remain in close agreement with the experimental profiles over the full temperature range.

For ^{2}NO, differences among mechanisms become more apparent at temperatures above approximately 1200 K. The NUIG_2023 and Shrestha_2025 mechanisms predict significantly higher ^{2}NO concentrations than observed experimentally, whereas the Zhang_2023 mechanism yields ^{2}NO levels comparable to those predicted by the RMG-based models.

For N_2O, only the Zhang_2023 mechanism provides reasonable agreement with the experimental measurements, while all other mechanisms substantially overpredict the peak N_2O mole fraction. Similar to the pure-NH_3 case, these discrepancies highlight ongoing uncertainties in N_2O formation and consumption pathways, which are not alleviated by the addition of modest amounts of H_2.

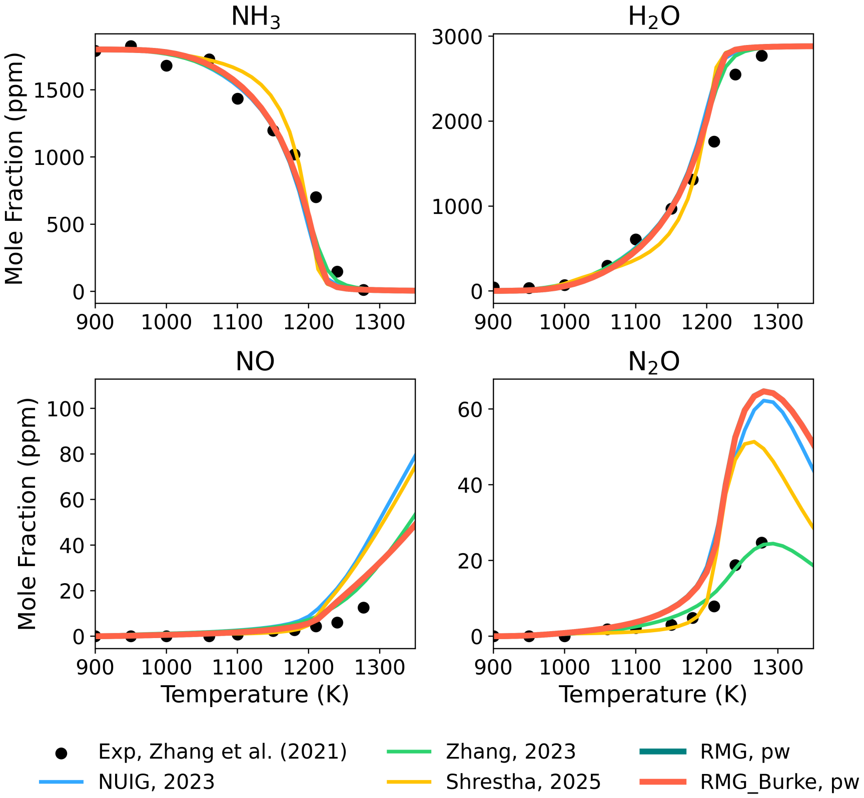

Figure S13: RMG-generated mechanism and representative literature mechanisms [44–46] comparisons against species profiles in JSR oxidation of 90%NH_3/10%H_2 mixture [60].

8.4. Oxidation in a Flow Reactor (FR)

Figure S14 compares simulated species profiles from the RMG-based mechanisms and representative literature mechanisms with experimental measurements for flow-reactor (FR) oxidation of pure NH_3 (solid lines) and a 50 % NH_3 / 50 % H_2 mixture (dashed lines).

For pure NH_3, the Shrestha_2025 mechanism predicts the closest agreement with the experimental onset temperature for NH_3 consumption, whereas the RMG and RMG Burke mechanisms exhibit a slightly higher-temperature onset. In contrast, the NUIG_2023 and Zhang_2023 mechanisms predict earlier NH_3 consumption than observed experimentally. For O_2, N_2, and H_2O, the RMG and RMG Burke mechanisms provide the closest overall agreement with the experimental onset and temperature dependence. The remaining literature mechanisms generally predict earlier consumption or formation, corresponding to lower onset temperatures than observed. For ^{2}NO, the RMG-based mechanisms

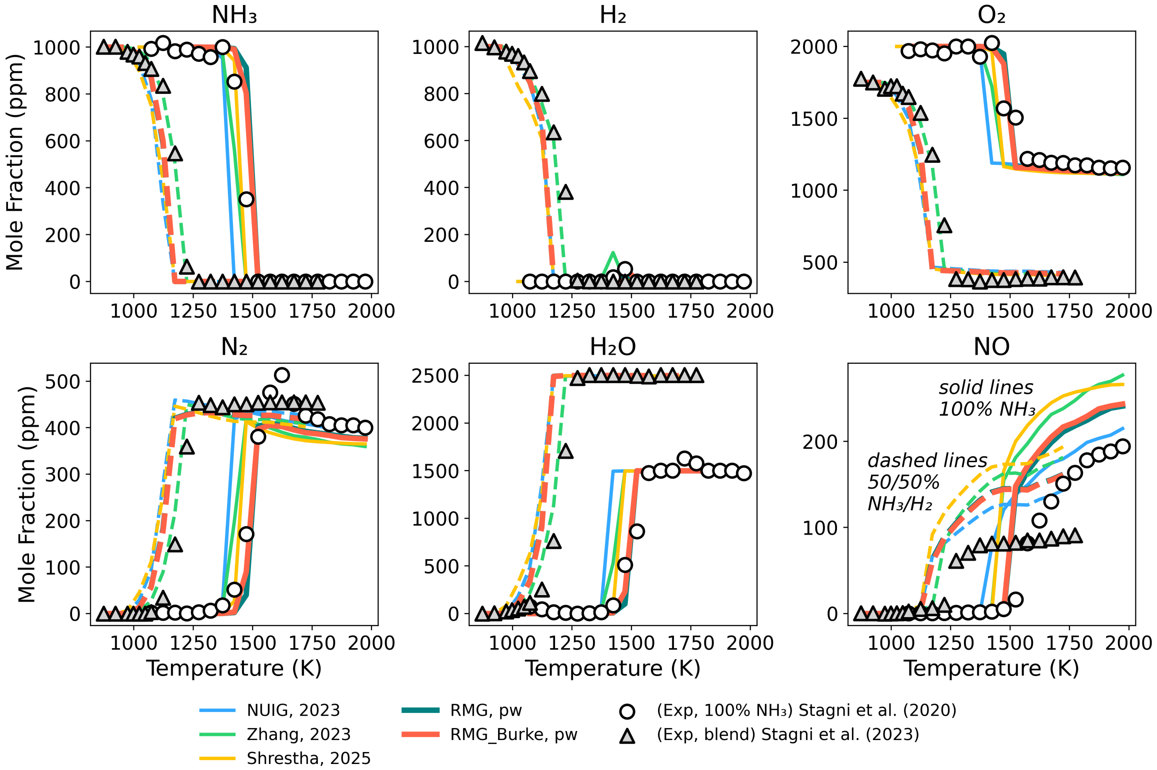

Figure S14: Comparisons of RMG-generated mechanisms and representative literature mechanisms [44–46] against experimental species profiles in Flow Reactor (FR) oxidations; pure NH_3 (solid line) [62] and 50 %NH_3/50 %H_2 mixture (dashed line) [63].

reproduce the experimental onset temperature most closely. However, all mechanisms substantially overpredict ^{2}NO concentrations at temperatures above approximately 1500 K, indicating persistent deficiencies in describing high-temperature ^{2}NO formation and recycling under FR conditions.

Under blended-fuel conditions, differences among mechanisms become more pronounced. For the major reactants and products (NH_3, H_2, O_2, N_2, and H_2O), the Zhang_2023 mechanism provides the closest overall agreement with the experimental profiles in terms of both onset temperature and species concentration. The RMG and RMG Burke mechanisms yield comparable trends but exhibit larger deviations in onset for several species. For ^{2}NO, all mechanisms continue to overpredict the measured concentrations across the entire temperature range, similar to the pure-NH_3 case. The addition of H_2 does not alleviate this discrepancy, underscoring the continued challenges associated with ^{2}NO-forming pathways in NH_3/H_2 oxidation under flow-reactor conditions.

Overall, the FR results indicate that the inclusion of H_2 amplifies differences among kinetic models that are otherwise indistinguishable under pure-NH_3 conditions. While most mechanisms reproduce the main qualitative trends, quantitative discrepancies persist under blended-fuel conditions, highlighting the increased sensitivity of NH_3/H_2 oxidation to detailed kinetic treatment in flow-reactor environments.

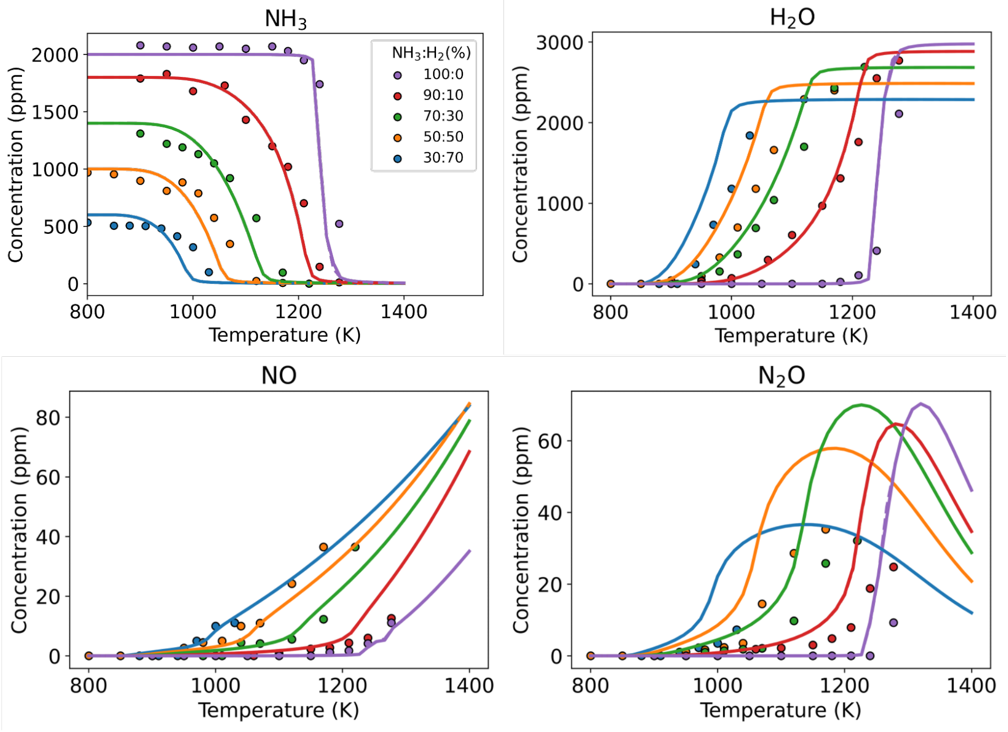

Figure S15: Comparison of simulated species profiles from the RMG (solid lines) and RMG_Burke (dashed lines) models with experimental data for NH_3/H_2 oxidation in a jet-stirred reactor at various blending ratios.[60]

9. Blending effects of H_2 on NH_3 oxidation

9.1. Jet-Stirred Reactor (JSR) simulations

Overall, the RMG_Burke and RMG models yield nearly indistinguishable predictions across most NH_3/H_2 blending ratios and species, as evidenced by the close overlap between the solid and dashed lines in Fig. S15. The addition of H_2 systematically promotes earlier ignition, leading to combustion initiation at lower temperatures for all mixtures.

For NH_3 consumption and H_2O formation, both mechanisms capture the main temperature-dependent trends across all blending ratios. The agreement with experiment is generally strongest under pure-NH_3 conditions and remains reasonable for the blending conditions. For ^2NO, the best agreement between model predictions and experimental data is observed for pure NH_3 and $30\,\%\,NH_3\,/\,70\,\%\,H_2$ mixture. For N_2O, both the RMG and RMG_Burke mechanisms show poor quantitative agreement with the measurements across all blending ratios, substantially overpredicting the peak of N_2O mole fractions. This behavior suggests that uncertainties in N_2O-forming and -consuming reaction pathways persist and are not alleviated by H_2 addition.

Overall, the model performance is consistently best under pure-NH_3 conditions, while the inclusion of H_2 amplifies discrepancies, highlighting the continued need for refinement of nitrogen chemistry in NH_3/H_2 oxidation systems.

9.2. Flow Reactor (FR) simulations

As shown in Figure S16, the RMG_Burke model performs similarly to the base RMG model in reproducing the experimental data across most NH_3/H_2 blending ratios and species. In many cases, the solid (RMG) and dashed (RMG_Burke) curves nearly overlap, indicating that the two mechanisms yield essentially indistinguishable predictions under the present flow-reactor conditions.

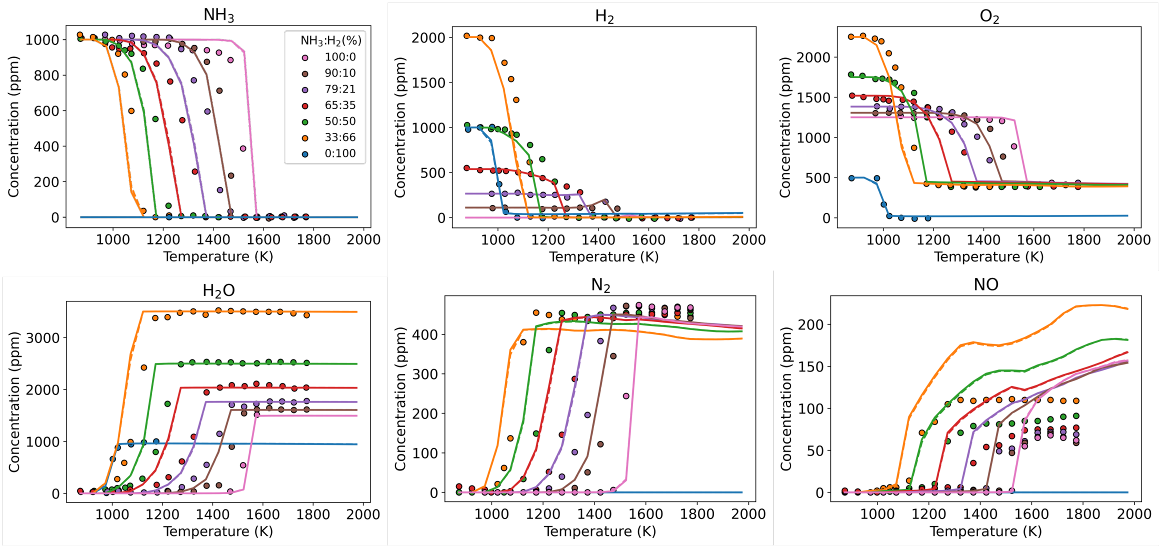

Figure S16: Comparison of simulated species profiles from the RMG (solid lines) and RMG_Burke (dashed lines) models with experimental data for NH_3/H_2 oxidation in a flow reactor at various blending ratios.[63]

Under pure-H_2 conditions, both mechanisms provide the best overall agreement with the experimental measurements. For the major reactants (NH_3, H_2, and O_2) and the products (H_2O and N_2), the models generally capture the consumption and formation trends reasonably well across all conditions examined.

In contrast, ^{2}NO remains systematically overpredicted under all conditions. At higher temperatures, the predicted ^{2}NO concentrations can exceed the experimental values by approximately a factor of two. This consistent overprediction indicates persistent challenges in accurately describing ^{2}NO-forming and recycling pathways, particularly in the high-temperature regime.

10. Rate of Production (ROP) Analysis in pure NH_3 JSR simulations

To reveal the major pathways for ^2NO (Figure S17) and N_2O (Figure S18) generation, we conducted ROP analyses and compared them across seven mechanisms: RMG, RMG with the Burke rule[64], CRECK_2023[63], NUIG_2024[65], KAUST_2021[60], KAUST_2023[45], and KAUST_2024[66]. The analyses were conducted under the same JSR conditions as those used for the pure NH_3 speciation profiles at 1300 K (Fig. 10).

For ^2NO, all mechanisms predict similar qualitative pathways, with the production and consumption fluxes (10^{-5} mol cm^{-3} s^{-1}) being roughly two orders of magnitude larger than the net rate of ^2NO formation (10^{-7} mol cm^{-3} s^{-1}). This indicates that ^2NO is a highly recycled intermediate, and small variations in individual reaction rates have limited impact on its steady-state concentration. Among the mechanisms, only CRECK_2023 shows a noticeably different overall balance compared to the others.

In terms of formation, HNO decomposition is the dominant route for all mechanisms considered:

$$\mathrm{HNO} \longrightarrow \mathrm{H} + {}^2\mathrm{NO},$$

This channel consistently contributes a significant fraction of the total ^2NO production flux, although its relative importance varies moderately among mechanisms.

For ^2NO consumption, all mechanisms except KAUST_2024 identify $^2NH_2 + {}^2NO \longrightarrow N_2 + H_2O$ as the primary sink. KAUST_2024, however, predicts that $^3NH + {}^2NO \longrightarrow H + N_2O$ dominates instead. This shift likely arises from updated rate coefficients in the KAUST_2024 mechanism for the competing reactions $^2NH_2 + {}^2NO \longrightarrow {}^2NNH + {}^2OH$ and $^2NH_2 + {}^2NO \longrightarrow N_2 + H_2O$.

For N_2O, the production, consumption, and net rates are in the comparable order of magnitudes, indicating a near steady-state balance between its formation and destruction pathways. Among the mechanisms, KAUST_2024 exhibits noticeably higher absolute rates of both N_2O production and consumption, consistent with its overall overprediction of N_2O concentrations in the JSR simulations.

Across all mechanisms, N_2O formation is almost exclusively dominated by the recombination reaction

$$^3\mathrm{NH} + {}^2\mathrm{NO} \longrightarrow \mathrm{H} + \mathrm{N_2O},$$

whose rate constant was updated in the KAUST_2024 model. The higher rate in KAUST_2024 for this channel likely contributes to its enhanced N_2O production.

For N_2O consumption, the most influential reaction in all mechanisms is

$$\mathrm{H} + \mathrm{N_2O} \longrightarrow \mathrm{N_2} + {}^2\mathrm{OH},$$

followed by N_2O (+M) $\longrightarrow$ N_2 + O (+M) and $N_2H_2 + {}^2NO \longrightarrow N_2O + {}^2NH_2$. While these three reactions dominate in most mechanisms, KAUST_2024 differs by featuring $N_2O + {}^3NH \longrightarrow HNO + N_2$ as its third-most important sink. This altered reaction balance likely explains the enhanced N_2O formation predicted by KAUST_2024 relative to other models.

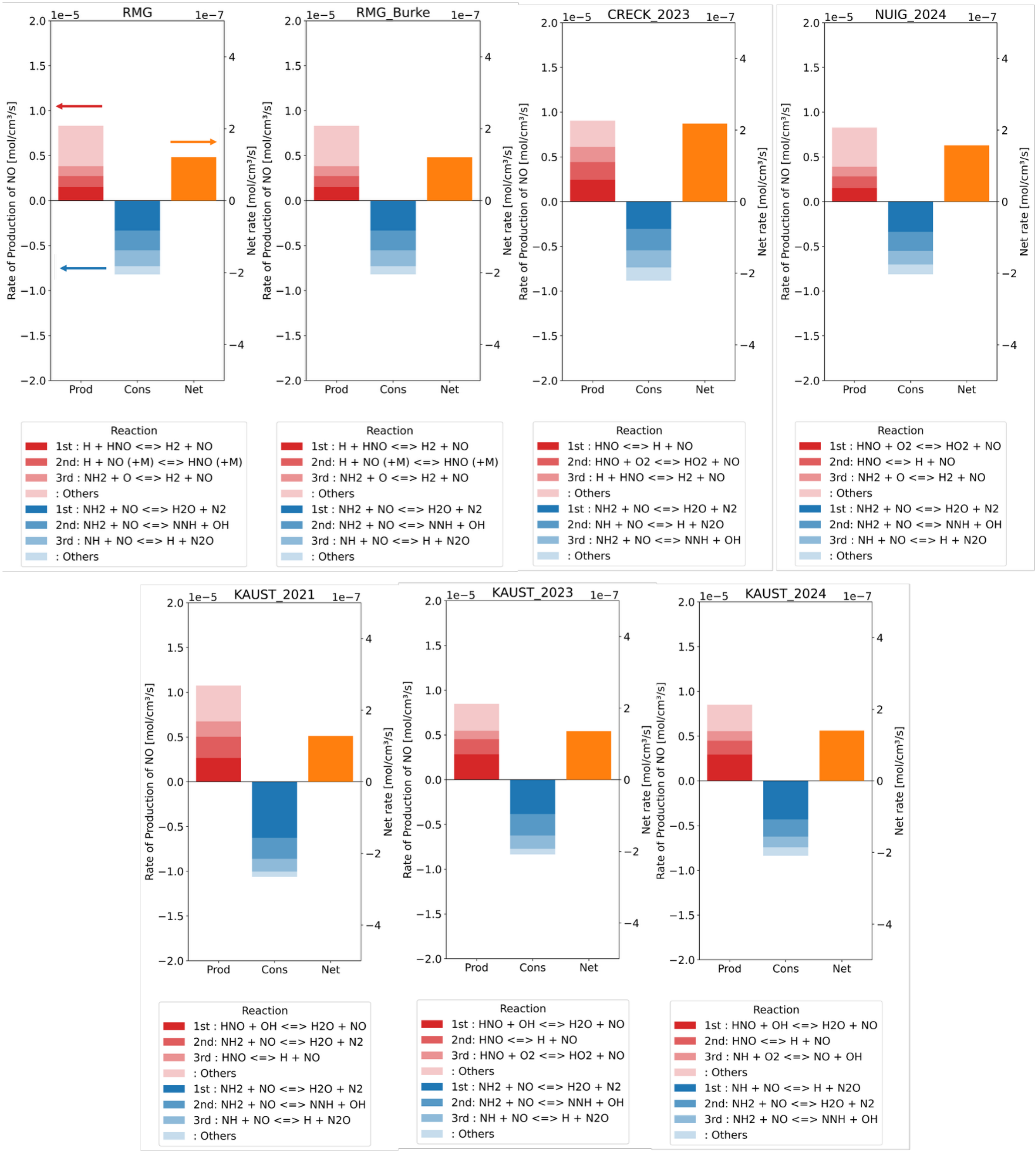

Figure S17: ROP Analysis for ^{2}NO species in pure NH_3 JSR simulations

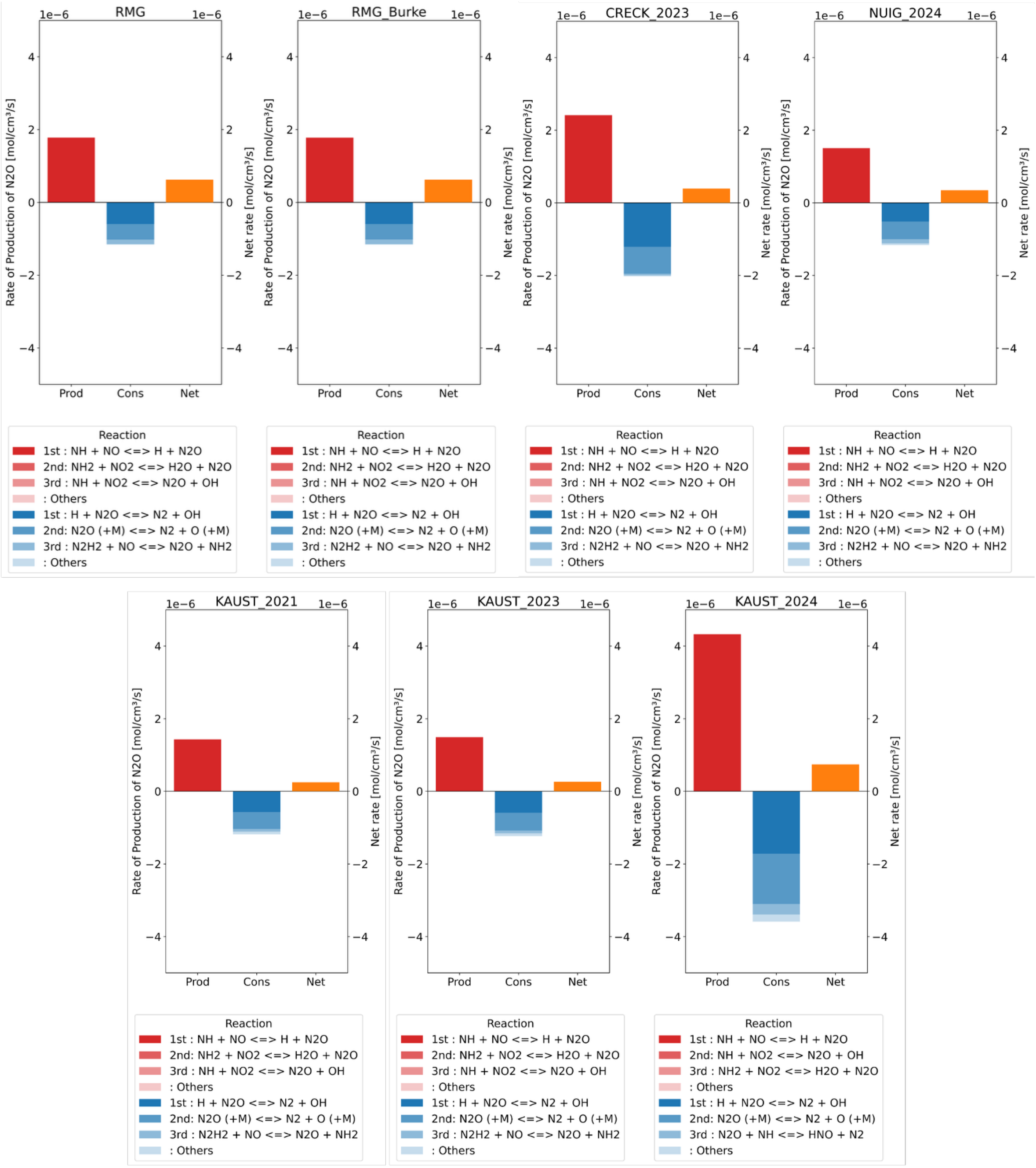

Figure S18: ROP Analysis for N_2O species in pure NH_3 JSR simulations

11. Troe parameterizations of the six reactions treated with linear mixture rule in reduced pressure.

We tabulate below in Table S3 the Troe parametrizations of reactions R1–6. Figure S19 depicts how the classical and linear-mixture rule in reduced pressure rate coefficients deviate in mixed bath gases as reactions enter the fall-off region.

Table S3: Troe parametrizations of the six reactions treated with the linear mixture rule in reduced pressure (LMR-R). These parametrizations are for the reference reactions. Temperature-dependent third-body efficiencies for other bath gases were taken from Jasper [67].

$\mathrm{H} + {}^{2}\mathrm{OH}\,(+\mathrm{N_2}) \rightleftharpoons \mathrm{H_2O}\,(+\mathrm{N_2})$	Reference
$k_0, A = 4.53 \cdot 10^{21}\ \mathrm{cm^6\ mol^{-2}\ s^{-1}}, n = -1.81, E_\mathrm{a} = 0.499\ \mathrm{kcal\ mol^{-1}}$	[68]
$k_\infty, A = 2.51 \cdot 10^{13}\ \mathrm{cm^3\ mol^{-1}\ s^{-1}}, n = 0.234, E_\mathrm{a} = -0.114\ \mathrm{kcal\ mol^{-1}}$	[68]
$\alpha = 0.73, T_3 = 1.0 \cdot 10^{-30}\ \mathrm{K}, T_1 = 1.0 \cdot 10^{30}\ \mathrm{K}, T_2 = 1.0 \cdot 10^{30}\ \mathrm{K}$	[68]
$\mathrm{H} + {}^{3}\mathrm{O_2}\,(+\mathrm{Ar}) \rightleftharpoons {}^{2}\mathrm{HO_2}\,(+\mathrm{Ar})$	Reference
$k_0, A = 1.225 \cdot 10^{19}\ \mathrm{cm^6\ mol^{-2}\ s^{-1}}, n = -1.2, E_\mathrm{a} = 0.0$	[69]
$k_\infty, A = 4.66 \cdot 10^{12}\ \mathrm{cm^3\ mol^{-1}\ s^{-1}}, n = 0.44, E_\mathrm{a} = 0.0$	[69]
$\alpha = 0.0, T_3 = 1.75 \cdot 10^{3}\ \mathrm{K}, T_1 = 1.0 \cdot 10^{-10}\ \mathrm{K}, T_2 = 1.0 \cdot 10^{30}\ \mathrm{K}$	[69]
$\mathrm{H_2O_2}\,(+\mathrm{Ar}) \rightleftharpoons 2\,{}^{2}\mathrm{OH}\,(+\mathrm{Ar})$	Reference
$k_0, A = 2.49 \cdot 10^{24}\ \mathrm{cm^3\ mol^{-1}\ s^{-1}}, n = -2.3, E_\mathrm{a} = 48.75\ \mathrm{kcal\ mol^{-1}}$	[70]
$k_\infty, A = 2.0 \cdot 10^{12}\ \mathrm{s^{-1}}, n = 0.9, E_\mathrm{a} = 48.75\ \mathrm{kcal\ mol^{-1}}$	[70]
$\alpha = 0.42, T_3 = 1.0 \cdot 10^{30}\ \mathrm{K}, T_1 = 1.0 \cdot 10^{30}\ \mathrm{K}, -$	[70]
$\mathrm{H} + {}^{2}\mathrm{NH_2}\,(+\mathrm{N_2}) \rightleftharpoons \mathrm{NH_3}\,(+\mathrm{N_2})$	Reference
$k_0, A = 4.655 \cdot 10^{30}\ \mathrm{cm^6\ mol^{-2}\ s^{-1}}, n = -4.103, E_\mathrm{a} = 3.3145\ \mathrm{kcal\ mol^{-1}}$	[71]
$k_\infty, A = 1.5 \cdot 10^{14}\ \mathrm{cm^3\ mol^{-1}\ s^{-1}}, n = 0.167, E_\mathrm{a} = 0.0$	[72]
$\alpha = 0.492, T_3 = 1.664 \cdot 10^{2}\ \mathrm{K}, T_1 = 1.893 \cdot 10^{3}\ \mathrm{K}, T_2 = 6.07 \cdot 10^{3}\ \mathrm{K}$	[73]
$\mathrm{N_2H_4}\,(+\mathrm{Ar}) \rightleftharpoons 2\,{}^{2}\mathrm{NH_2}\,(+\mathrm{Ar})$	Reference
$k_0, A = 4.845 \cdot 10^{42}\ \mathrm{cm^3\ mol^{-1}\ s^{-1}}, n = -7.3, E_\mathrm{a} = 68.54\ \mathrm{kcal\ mol^{-1}}$	[74]
$k_\infty, A = 7.6 \cdot 10^{19}\ \mathrm{s^{-1}}, n = -1.0, E_\mathrm{a} = 66.77\ \mathrm{kcal\ mol^{-1}}$	[74]
$\alpha = 0.29, T_3 = 1.460 \cdot 10^{3}\ \mathrm{K}, T_1 = 2.1 \cdot 10^{1}\ \mathrm{K}, T_2 = 1.34 \cdot 10^{4}\ \mathrm{K}$	[74]
$\mathrm{H} + {}^{2}\mathrm{NO}\,(+\mathrm{N_2}) \rightleftharpoons \mathrm{HNO}\,(+\mathrm{N_2})$	Reference
$k_0, A = 1.230 \cdot 10^{21}\ \mathrm{cm^6\ mol^{-2}\ s^{-1}}, n = -1.912, E_\mathrm{a} = -0.3957\ \mathrm{kcal\ mol^{-1}}$	[71]
$k_\infty, A = 1.500 \cdot 10^{15}\ \mathrm{cm^3\ mol^{-1}\ s^{-1}}, n = -0.410, E_\mathrm{a} = 0.0$	[75]
$\alpha = 0.623, T_3 = 6.625 \cdot 10^{3}\ \mathrm{K}, T_1 = 1.867 \cdot 10^{2}\ \mathrm{K}, T_2 = 4.659 \cdot 10^{3}\ \mathrm{K}$	[73]

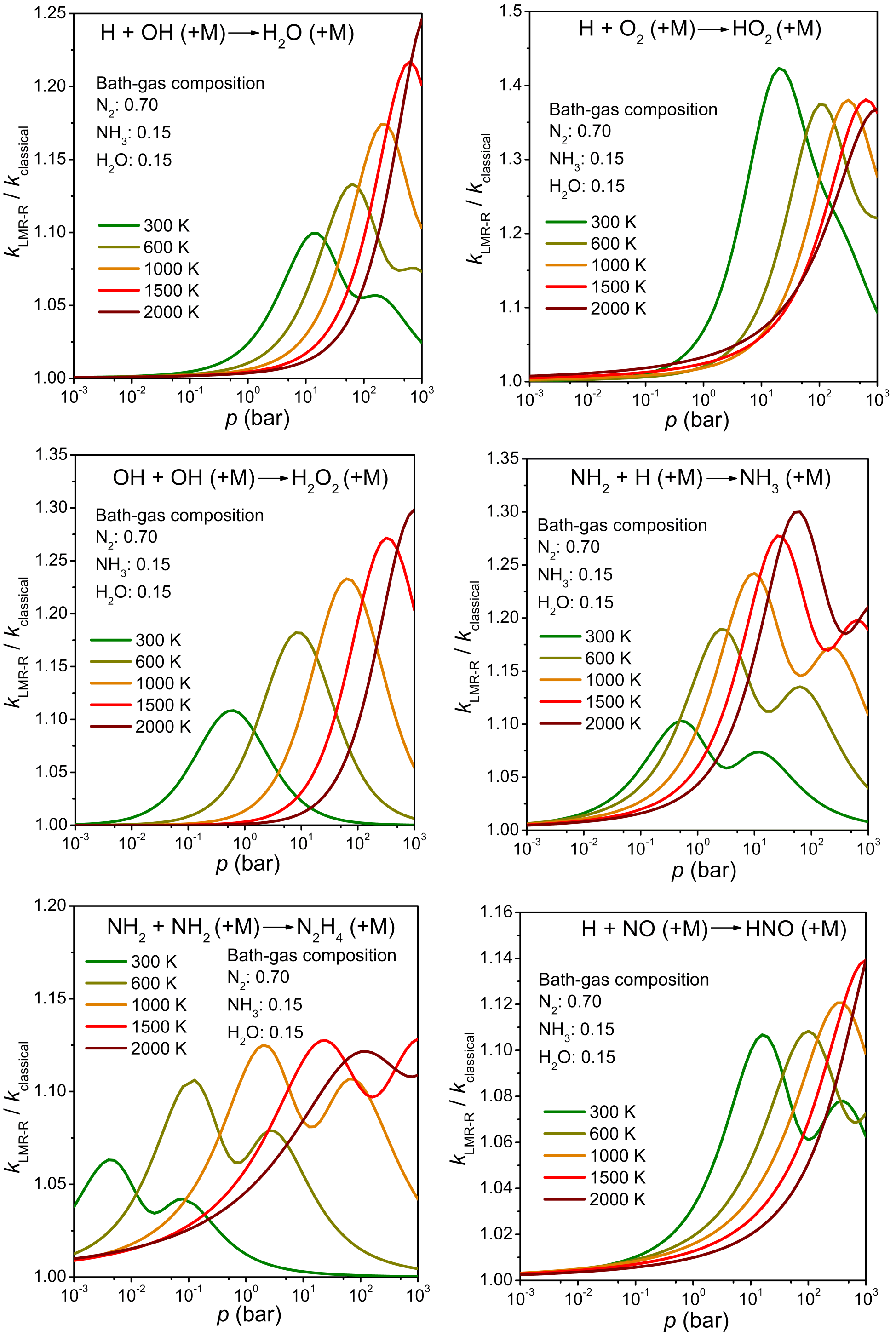

Figure S19: This figure depicts how the mixed-bath-gas rate coefficient predicted by the classical and the linear-mixture rule in reduced pressure deviate for six reactions in the fall-off region

References

[1] M. Liu, A. Grinberg Dana, M. S. Johnson, M. J. Goldman, A. Jocher, A. M. Payne, C. A. Grambow, K. Han, N. W. Yee, E. J. Mazeau, K. Blondal, R. H. West, C. F. Goldsmith and W. H. Green, *J. Chem. Inf. Model.*, 2021, **61**, 2686–2696.

[2] M. S. Johnson, X. Dong, A. Grinberg Dana, Y. Chung, D. J. Farina, R. J. Gillis, M. Liu, N. W. Yee, K. Blondal, E. Mazeau, C. A. Grambow, A. M. Payne, K. A. Spiekermann, H.-W. Pang, C. F. Goldsmith, R. H. West and W. H. Green, *J. Chem. Inf. Model.*, 2022, **62**, 4906–4915.

[3] *RMG-database - A chemistry database for RMG*, `https://github.com/ReactionMechanismGenerator/RMG-database`.

[4] C. Eckart, *Physical Review*, **35**, 1303–1309.

[5] H. S. Johnston and J. Heicklen, *The Journal of Physical Chemistry*, **66**, 532–533.

[6] A. G. Dana, M. S. Johnson, J. W. Allen, S. Sharma, S. Raman, M. Liu, C. W. Gao, C. A. Grambow, M. J. Goldman, D. S. Ranasinghe, R. J. Gillis, A. M. Payne, Y.-P. Li, X. Dong, K. A. Spiekermann, H. Wu, E. E. Dames, Z. J. Buras, N. M. Vandewiele, N. W. Yee, S. S. Merchant, B. Buesser, C. A. Class, F. Goldsmith, R. H. West and W. H. Green, *International Journal of Chemical Kinetics*, 2023, **55**, 300–323.

[7] M. J. Frisch *et al.*, *Gaussian 16 Revision B.01*, 2016, Gaussian Inc. Wallingford CT.

[8] H.-J. Werner, P. J. Knowles, G. Knizia, F. R. Manby and M. Schütz, *WIREs Computational Molecular Science*, 2012, **2**, 242–253.

[9] H.-J. Werner, P. J. Knowles, F. R. Manby, J. A. Black, K. Doll, A. Heßelmann, D. Kats, A. Köhn, T. Korona, D. A. Kreplin, Q. Ma, I. Miller, Thomas F., A. Mitrushchenkov, K. A. Peterson, I. Polyak, G. Rauhut and M. Sibaev, *The Journal of Chemical Physics*, 2020, **152**, 144107.

[10] J.-D. Chai and M. Head-Gordon, *Phys. Chem. Chem. Phys.*, 2008, **10**, 6615–6620.

[11] F. Weigend and R. Ahlrichs, *Phys. Chem. Chem. Phys.*, 2005, **7**, 3297–3305.

[12] T. H. Dunning, *J. Chem. Phys.*, 1989, **90**, 1007–1023.

[13] C. Kollmar, K. Sivalingam, Y. Guo and F. Neese, *The Journal of Chemical Physics*, 2021, **155**, 234104.

[14] J. D. Watts, J. Gauss and R. J. Bartlett, *J. Chem. Phys.*, 1993, **98**, 8718–8733.

[15] M. Kállay and J. Gauss, *The Journal of Chemical Physics*, 2008, **129**, 144101.

[16] F. Neese, *Wiley Interdiscip. Rev. Comput. Mol. Sci.*, 2012, **2**, 73–78.

[17] M. Kállay, P. R. Nagy, D. Mester, Z. Rolik, G. Samu, J. Csontos, J. Csóka, P. B. Szabó, L. Gyevi-Nagy, B. Hégely, I. Ladjánszki, L. Szegedy, B. Ladóczki, K. Petrov, M. Farkas, P. D. Mezei and Á. Ganyecz, *The Journal of Chemical Physics*, 2020, **152**, 074107.

[18] MRCC, a quantum chemical program suite written by M. Kállay, P. R. Nagy, D. Mester, L. Gyevi-Nagy, J. Csóka, P. B. Szabó, Z. Rolik, G. Samu, J. Csontos, B. Hégely, Á. Ganyecz, I. Ladjánszki, L. Szegedy, B. Ladóczki, K. Petrov, M. Farkas, P. D. Mezei, and R. A. Horváth. See www.mrcc.hu.

[19] S. Kanchanakungwankul, J. L. Bao, J. Zheng, I. M. Alecu, B. J. Lynch, Y. Zhao, and D. G. Truhlar, 2021, `https://comp.chem.umn.edu/freqscale/210722_Database_of_Freq_Scale_Factors_v5.pdf`.

[20] A. Halkier, T. Helgaker, P. Jørgensen, W. Klopper, H. Koch, J. Olsen and A. K. Wilson, *Chem. Phys. Lett.*, 1998, **286**, 243–252.

[21] A. Halkier, T. Helgaker, P. Jørgensen, W. Klopper and J. Olsen, *Chem. Phys. Lett.*, 1999, **302**, 437 – 446.

[22] T. Helgaker, W. Klopper, H. Koch and J. Noga, *J. Chem. Phys.*, 1997, **106**, 9639–9646.

[23] T. J. Lee and P. R. Taylor, *Int. J. Quantum Chem.*, 1989, **36**, 199–207.

[24] B. Ruscic and D. H. Bross, Active Thermochemical Tables (ATcT) values based on ver. 1.202 of the Thermochemical Network (2024); available at ATcT.anl.gov.

[25] D. R. Glowacki, C.-H. Liang, C. Morley, M. J. Pilling and S. H. Robertson, *J. Phys. Chem. A*, 2012, **116**, 9545–9560.

[26] J. T. Bartis and B. Widom, *J. Chem. Phys.*, 1974, **60**, 3474–3482.

[27] S. H. Robertson, M. J. Pilling, L. C. Jitariu and I. H. Hillier, *Phys. Chem. Chem. Phys.*, 2007, **9**, 4085–4097.

[28] Y. Georgievskii and S. J. Klippenstein, *J. Chem. Phys.*, 2003, **118**, 5442–5455.

[29] J. Zheng, J. L. Bao, S. Zhang, J. C. Corchado, R. Meana-Pañeda, Y.-Y. Chuang, E. L. Coitiño, B. A. Ellingson and D. G. Truhlar, *Gaussrate 17*, 2017, University of Minnesota.

[30] S. Inomata and N. Washida, *The Journal of Physical Chemistry A*, 1999, **103**, 5023–5031.

[31] X. Chen, M. E. Fuller and C. Franklin Goldsmith, *React. Chem. Eng.*, 2019, **4**, 323–333.

[32] B. E. Poling, J. M. Prausnitz and J. P. O'Connell, *The Properties of Gases and Liquids*, McGraw-Hill, 5th edn, 2001.

[33] H.-J. Werner, P. J. Knowles *et al.*, *MOLPRO, version , a package of ab initio programs*, see.

[34] P. Celani and H.-J. Werner, *The Journal of Chemical Physics*, 2000, **112**, 5546–5557.

[35] S. J. Klippenstein, L. B. Harding, B. Ruscic, R. Sivaramakrishnan, N. K. Srinivasan, M.-C. Su and J. V. Michael, *The Journal of Physical Chemistry A*, 2009, **113**, 10241–10259.

[36] S. H. Robertson, D. M. Wardlaw and A. F. Wagner, *The Journal of Chemical Physics*, 2002, **117**, 593–605.

[37] J. W. Davies, N. J. Green and M. J. Pilling, *Chem. Phys. Lett.*, 1986, **126**, 373–379.

[38] W. Forst, *J. Phys. Chem.*, 1972, **76**, 342–348.

[39] S. J. Klippenstein, L. B. Harding, P. Glarborg and J. A. Miller, *Combustion and Flame*, **158**, 774–789.

[40] P. Glarborg, J. A. Miller, B. Ruscic and S. J. Klippenstein, **67**, 31–68.

[41] S. Inomata and N. Washida, **103**, 5023–5031.

[42] *Gas-Phase Combustion Chemistry*, `http://link.springer.com/10.1007/978-1-4612-1310-9`.

[43] S. H. Mousavipour, F. Pirhadi and A. HabibAgahi, **113**, 12961–12971.

[44] G. Yin, B. Xiao, H. Zhan, E. Hu and Z. Huang, **249**, 112617.

[45] X. Zhang, K. K. Yalamanchi and S. Mani Sarathy, *Fuel*, 2023, **341**, 127676.

[46] K. P. Shrestha, B. R. Giri, R. Pelé, K. Aljohani, P. Brequigny, F. Mauss, F. Halter, L. K. Huynh and C. Mounaïm-Rousselle, **274**, 113954.

[47] O. Mathieu and E. L. Petersen, *Combust. Flame*, 2015, **162**, 554–570.

[48] J. Chen, X. Jiang, X. Qin and Z. Huang, *Fuel*, 2021, **287**, 119563.

[49] P. D. Ronney, *Combust. Sci. Technol.*, 1988, **59**, 123–141.

[50] U. Pfahl, M. Ross, J. Shepherd, K. Pasamehmetoglu and C. Unal, *Combust. Flame*, 2000, **123**, 140–158.

[51] T. Jabbour and D. F. Clodic, *ASHRAE Trans.*, 2004, **110**, 522–533.

[52] A. Hayakawa, T. Goto, R. Mimoto, Y. Arakawa, T. Kudo and H. Kobayashi, *Fuel*, 2015, **159**, 98–106.

[53] K. Takizawa, A. Takahashi, K. Tokuhashi, S. Kondo and A. Sekiya, *J. Hazard. Mater.*, 2008, **155**, 144–152.

[54] A. Ichikawa, A. Hayakawa, Y. Kitagawa, K. Kunkuma Amila Somarathne, T. Kudo and H. Kobayashi, *Int. J. Hydrog. Energy*, 2015, **40**, 9570–9578.

[55] B. L. . W. G. Yanchao Li, Mingshu Bi, *Combust. Sci. Technol.*, 2018, **190**, 1804–1816.

[56] B. Mei, X. Zhang, S. Ma, M. Cui, H. Guo, Z. Cao and Y. Li, *Combust. Flame*, 2019, **210**, 236–246.

[57] X. Han, Z. Wang, M. Costa, Z. Sun, Y. He and K. Cen, *Combust. Flame*, 2019, **206**, 214–226.

[58] K. P. Shrestha, C. Lhuillier, P. B. Amanda Alves Barbosa, F. Contino, C. Mounaïm-Rousselle, L. Seidel and F. Mauss, *Proc. Combust. Inst.*, 2021, **38**, 2163–2174.

[59] C. Lhuillier, P. Brequigny, N. Lamoureux, F. Contino and C. Mounaïm-Rousselle, *Fuel*, 2020, **263**, 116653.

[60] X. Zhang, S. P. Moosakutty, R. P. Rajan, M. Younes and S. M. Sarathy, *Combust. Flame*, 2021, **234**, 111653.

[61] K. N. Osipova, X. Zhang, S. M. Sarathy, O. P. Korobeinichev and A. G. Shmakov, *Fuel*, 2022, **310**, 122202.

[62] A. Stagni, C. Cavallotti, S. Arunthanayothin, Y. Song, O. Herbinet, F. Battin-Leclerc and T. Faravelli, *React. Chem. Eng.*, 2020, **5**, 696–711.

[63] A. Stagni, S. Arunthanayothin, M. Dehue, O. Herbinet, F. Battin-Leclerc, P. Bréquigny, C. Mounaïm-Rousselle and T. Faravelli, *Chem. Eng. J.*, 2023, **471**, 144577.

[64] P. J. Singal, J. Lee, L. Lei, R. L. Speth and M. P. Burke, *Proc. Combust. Inst.*, 2024, **40**, 105779.

[65] Y. Zhu, H. J. Curran, S. Girhe, Y. Murakami, H. Pitsch, K. Senecal, L. Yang and C.-W. Zhou, *Combust. Flame*, 2024, **260**, 113239.

[66] M. Monge-Palacios, X. Zhang, N. Morlanes, H. Nakamura, G. Pezzella and S. M. Sarathy, *Prog. Energy Combust. Sci.*, 2024, **105**, 101177.

[67] A. Jasper, *Faraday Discuss.*, 2022, **238**, 68–86.

[68] S. R. Sellevåg, Y. Georgievskii and J. A. Miller, *The Journal of Physical Chemistry A*, 2008, **112**, 5085–5095.

[69] A. A. Konnov, *Combustion and Flame*, 2019, **203**, 14–22.

[70] A. A. Konnov, *Combustion and Flame*, 2015, **162**, 3755–3772.

[71] A. Stagni, C. Cavallotti, S. Arunthanayothin, Y. Song, O. Herbinet, F. Battin-Leclerc and T. Faravelli, *React. Chem. Eng.*, 2020, **5**, 696–711.

[72] P. Glarborg, H. Hashemi and P. Marshall, *Fuel Communications*, 2022, **10**, 100049.

[73] A. Stagni and T. Dinelli, *Chemical Engineering Journal*, 2025, **526**, 170737.

[74] P. Glarborg, H. Hashemi, S. Cheskis and A. W. Jasper, *The Journal of Physical Chemistry A*, 2021, **125**, 1505–1516.

[75] W. Tsang and J. T. Herron, *Journal of Physical and Chemical Reference Data*, 1991, **20**, 609–663.